DECOHERENCE AND ADIABATIC TRANSPORT IN SEMICONDUCTOR QUANTUM DOTS

A DISSERTATION

SUBMITTED TO THE DEPARTMENT OF PHYSICS

AND THE COMMITTEE ON GRADUATE STUDIES

OF STANFORD UNIVERSITY

IN PARTIAL FULFILLMENT OF THE REQUIREMENTS

FOR THE DEGREE OF

DOCTOR OF PHILOSOPHY

Michael Switkes

November 1999

I certify that I have read this dissertation and that in my opinion it is fully adequate, in scope and quality, as a dissertation for the degree of Doctor of Philosophy.

_____
Charles M. Marcus
(Principal Adviser)

I certify that I have read this dissertation and that in my opinion it is fully adequate, in scope and quality, as a dissertation for the degree of Doctor of Philosophy.

_____
Kathryn A. Moler

I certify that I have read this dissertation and that in my opinion it is fully adequate, in scope and quality, as a dissertation for the degree of Doctor of Philosophy.

_____
Paul L. McEuen

Approved for the University Committee on Graduate Studies:

_____

Abstract

I present research on ballistic electron transport in lateral GaAs/AlGaAs quantum dots connected to the environment with leads supporting one or more fully transmitting quantum modes. The first part of this dissertation examines electron the phenomena which mediate the transition from quantum mechanical to classical behavior in these quantum dots. Measurements of electron phase coherence time based on the magnitude of weak localization correction are presented as a function both of temperature and of applied bias. The coherence time is found to depend on temperature approximately as a sum of two power laws, $\tau_\phi \approx AT^{-1} + BT^{-2}$, in agreement with the prediction for *diffusive two dimensional* systems but not with predictions for closed quantum dots or ballistic 2D systems. The effects of a large applied bias can be described with an elevated effective electron temperature calculated from the balance of Joule heating and cooling by Wiedemann-Franz out diffusion of hot electrons. The limits this imposes for quantum dot based technologies are examined through the detailed analysis of a quantum dot magnetometer.

The second part of the work presented here focuses on a novel form of electron transport, adiabatic quantum electron pumping, in which a current is driven by cyclic changes in the wave function of a mesoscopic system rather than by an externally imposed bias. After a brief review of other mechanisms which produce a dc current from an ac excitation, measurements of adiabatic pumping are presented. The pumped current (or voltage) is sinusoidal in the phase difference between the two ac voltages deforming the dot potential and fluctuates in both magnitude and direction with small changes in external parameters such as magnetic field. Dependencies of pumping on the strength of the deformations, temperature, and breaking of time-reversal symmetry are also investigated.

Acknowledgements

I would first like to acknowledge the sources of funding without whose support none of this research would have been possible. The experiments described in this dissertation were carried out under grants from the A. P. Sloan Foundation, the Army Research Office, the National Science Foundation, and the Office of Naval Research.

Beyond financial support, the support of theorists and other experimentalists willing to think deeply about your experiment is invaluable as no experiment can exist in an intellectual vacuum. To that end, I would like to thank Borris Spivak and Fei Zhou who put me on the trail of adiabatic pumping and were very helpful in encouraging and correcting my understanding of it as our experiments progressed as well as Piet Brouwer who provided the random matrix theoretical framework for analysis of both the dephasing and adiabatic pumping measurements. Conversations with many other theorists including Igor Aleiner, Borris Altshuler, and Asa Auerbach also contributed to my understanding of these phenomena. Many experimentalists including Pierre Echternach, Andrei Geim, Michael Gershenson, Laurens Molenkamp, Dan Prober, and Michael Roukes contributed valuable ideas and advice to this work. In addition, I would like to thank our collaborators in the group of Arthur Gossard at UCSB, particularly Ken Campman and Kevin Mirnowski who provided the heterostructure wafers used in these experiments.

The most important scientific support system that underlies this work is the Marcus group at Stanford. All of the members of the group during my tenure, the graduate students Sara Cronenwett, Joshua Folk, Andy Huibers, Sebastian Maurer, Sam Patel, Mark Peterman, Duncan Stewart, and Dominik Zumbhul, the undergraduates Kevin Birnbaum, Steve Grossman, Fred Mancoff, Pam Olson, John Stockton, and Randy True, and the many visiting students have contributed to this dissertation with good ideas, experimental help, and their presence in the lab in the wee hours of the morning. I would particularly like to single out Andy Huibers with whom I worked closely at the beginning of my Ph.D. and

who was my collaborator on the dephasing measurements.

None of this work would have been possible without the constant input of ideas and perspective from my adviser Charlie Marcus. His intellectual rigor and experimental experience make him a great sounding board for scientific ideas and crazy experimental schemes, and his contacts in the physics community and promotion of our work consistently attract the top theorists in our field to think about our experiments.

I'd also like to thank the people who made this Ph.D. process possible for me personally. My parents who were thrilled to see me back in the Bay Area and who followed up with frequent dinner visits helped me keep the Ph.D. process in perspective and were a constant source of encouragement. Most importantly, however, is my wife Emma who agreed to marry me in the middle of this process and whose presence made this Ph.D. work along with everything else infinitely more meaningful.

Contents

Bibliography

Chapter 1

Introduction

1.1　Introduction

Electrical phenomena, particularly static electricity in the form of lightening, have fascinated and terrified humans for thousands of years. The scientific study of electricity, however, began only in the eighteenth and nineteenth centuries. Through three centuries of study, the physics of macroscopic electrical phenomena are quite well understood and form the field of *Classical Electrodynamics* [52]. Indeed, much of the technological progress of the present century stems from the understanding of such macroscopic electrical systems as lightbulbs and microwave antennas. Though quite different from classical electrodynamics, the physics of microscopic electron systems, for example a few electrons trapped in a spherically symmetric potential, is also well understood. These microscopic electrical systems, atoms, served as the experimental basis for the development of quantum mechanics in this century and are the object of some of the most precise and accurate theoretical calculations in all of physics [93].

This dissertation focuses on the physics of electrons at a size scale between micro- and macroscopic; mesoscopic physics covers systems small enough to exhibit quantum mechanical correlations and interference effects but large enough that concepts of average behavior remain valid. Mesoscopic electron systems have been the subject of study for over twenty years and the experiments presented here represent a second or third generation approach to the field. For general reviews of mesoscopic electron physics see [15] and [65].

The experimental system studied in this dissertation is the semiconductor quantum dot, a small semi-isolated conducting region embedded in a semiconducting host. The

size and shape of this region, the number of electrons it contains, and the strength of its connection to the environment are all determined by externally imposed electric fields created and shaped by metallic "gates" fabricated with lithographic techniques developed for the semiconductor industry (see appendix A). The combination of externally controlled electric fields and artificial fabrication provides great flexibility in device design, permitting many experiments which would be difficult or impossible in microscopic (atomic) systems. For example, atoms have a spherically symmetric central potential which gives rise to the well known features of atomic wave functions such as spherical harmonics, degenerate energy shells, magic numbers and so on. In contrast, the shape of the potential in a quantum dot is determined by the fabrication and the applied field, allowing arbitrary geometries which can be altered in situ. Quantum dots can thus be used to study the rules for quantum mechanics with any desired symmetry (such as the circular pancake in [104]) or the most general case of no symmetry at all (quantum chaos) as with the dots studied here. In addition, in situ control over the electron number allows experiments on quantum dots to address questions about the role of electron number and electron-electron interactions in quantum systems [100].

The work described in this dissertation focuses on two aspects of quantum dot physics. After an introduction in the remainder of this chapter, it goes on to examine decoherence, the process which transforms the quantum mechanics of the microscopic world into the classical mechanics of the macroscopic world. Chapter two presents measurements of the phase coherence time in quantum dots as a function of temperature along with background on decoherence processes and their theoretical treatment. Chapter three studies the effect of bias on decoherence and its implications for technological devices based on mesoscopic devices. A quantum dot magnetometer is analyzed in detail as an example.

The second part of the dissertation deals with adiabatic quantum pumping, a novel mechanism for transporting charge without an applied bias which, it is hoped, will be able to overcome the decoherence imposed limitations discussed in chapter three. Chapter four reviews some of the methods for transporting charge other than applying a bias. Chapter five describes measurements of adiabatic pumping in quantum dots and their theoretical interpretation.

Chapter six serves as a conclusion, summarizing the work and proposing future directions. Finally, there are three appendices which discuss the technical aspects of the experiments.
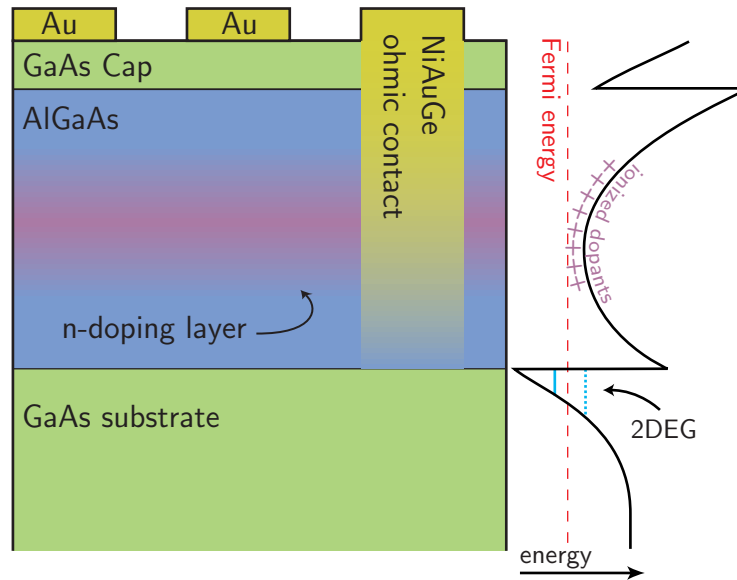
Figure 1.1: (left) Schematic diagram of a GaAs/AlGaAs heterostructure with Au Schottky gates deposited on the surface and an annealed NiAuGe ohmic contact. The purple region represents modulation doping of the AlGaAs with an n-type dopant, typically Si. (right) Conduction band energy diagram showing the well at the GaAs/AlGaAs interface which confines the 2DEG and its quantum energy levels. At low temperatures, only the lowest energy level in well is occupied.

The experiments described in chapters two and three were performed in collaboration with Andy Huibers and are also described in references [50] and [101] respectively. The work on adiabatic pumping is described in reference [102].

1.2 Creating Quantum Dots

A GaAs/Al$_{0.3}$Ga$_{0.7}$As heterostructure grown by molecular beam epitaxy (MBE) [47] serves as the semiconductor host for the quantum dots studied in this dissertation[*]. At low temperature, the heterostructure contains a very clean gas of electrons confined to a single plane from 30 to 200 nm below the semiconductor surface. This two dimensional electron gas (2DEG) is then further confined laterally to create quantum dots.

As its name implies, the heterostructure consists of several superimposed layers of GaAs

---

[*]The heterostructures were grown by Ken Campman and Kevin Maranowski in the group of Arthur Gossard at the University of California, Santa Barbara.

and AlGaAs as shown in Fig. 1.1. The 2D electron gas forms at the interface between the GaAs substrate and an undoped AlGaAs spacer layer grown on top. An n-type dopant is added, either as a single layer (δ-doping) or mixed with a layer of AlGaAs (modulation doping). A second layer of undoped AlGaAs and a GaAs cap layer (to prevent oxidation of the AlGaAs) complete the heterostructure. The thicknesses of the various layers can be adjusted to tune the properties of the 2DEG, such as mobility and electron density, over a wide range; one fairly typical heterostructure used had 30 nm of AlGaAs spacer, 15 nm of modulation doped AlGaAs, 10 nm of undoped AlGaAs, and 10 nm of GaAs cap, giving a 2DEG 65 nm below the surface. A full description of the heterostructures used in the experiments can be found in appendix B.

As the temperature of the heterostructure is lowered, electrons thermally ionized from the Si dopants become trapped at the heterointerface, prevented from recombining by the $\sim 0.3\,\mathrm{eV} \approx 25\,\mathrm{K}$ offset between conduction energies at the interface and from escaping into the GaAs by the electrostatic attraction of the ionized donors. At cryogenic temperatures the two dimensional character of the 2DEG is strengthened as the electrons populate only the lowest subband of the potential well while remaining free to move parallel to the interface. Because of the close match in lattice parameters between GaAs and AlGaAs ($\sim 7\%$ mismatch), the interface is only slightly strained and can be essentially defect free. Combined with the spatial separation of the 2DEG from the ionized donors, the scarcity of defects leads to a very low elastic scattering rate. The resulting high electron mobility $\mu_e \approx 10^5$–$10^6\,\mathrm{cm^2/Vs}$ and long mean free path[†] $\ell_e \approx 1$–$10\,\mu\mathrm{m}$ allow the fabrication of quantum dots in which electrons travel ballistically, scattering only from the (artificially fabricated) device boundaries.

At low temperature, the Schottky barrier between lithographically fabricated metal gates and the semiconductor surface prevents current from flowing when a negative voltage is applied to the gates. The electric field created by this voltage reduces the density of electrons in the 2DEG below (figure 1.2. A sufficiently large negative voltage ($\sim -1\,\mathrm{V}$) depletes the electron gas, forming an insulating region under the gate. Due to fringing fields, the insulating region extends beyond the edge of the gate a distance determined by the applied voltage, allowing in situ control of the size and shape of the dot. More precise control over the shape of the potential is possible using multiple independent gates to form a single wall of the dot. In dots with chaotic potentials, changing the voltages on these

---

[†]compared to $\sim 100\,\mathrm{nm}$ for Si MOSFETs and $\sim 10\,\mathrm{nm}$ for thin Au films
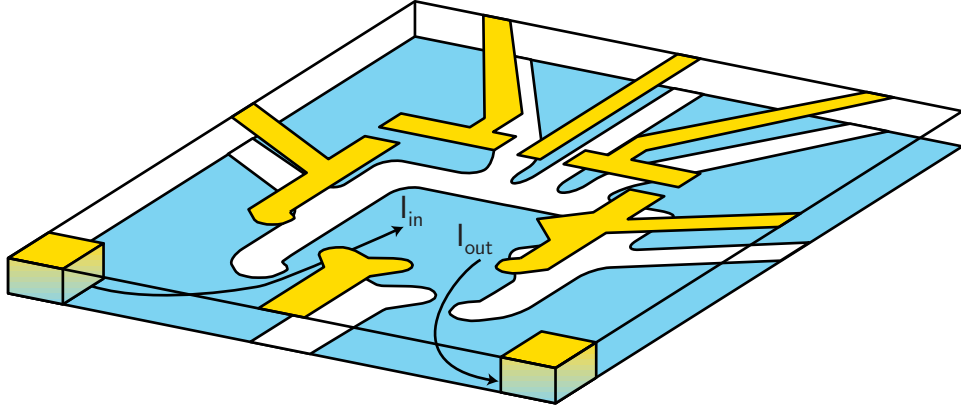
Figure 1.2: Negative voltage applied to Schottky gates on the surface (gold) depletes the 2DEG below (blue), creating an isolated quantum dot. Annealed NiAuGe squares make ohmic contact to the 2DEG.

"shape distortion gates" (figure 1.3) allows the measurement of an ensemble effectively different dots [24], a powerful and easily accessible technique for measuring the statistical properties of quantum dot behavior. Similarly, the strength of the dot's connection to the electron reservoirs can be controlled in situ by the voltages on the gates which define the point contact leads of the dot.

1.3 Basic Experimental Phenomena in Quantum Dots

1.3.1 Point Contacts and Coulomb Blockade

The simplest mesoscopic device is the point contact, a constriction in the 2DEG which opens smoothly to a wider region of electron gas on either end (see figure 1.4 inset). A quantum point contact is formed when the constriction is narrow enough to quantize the electron energy levels in the direction perpendicular to their flow, creating a 1D channel. Because the conductance is proportional to the Fermi velocity times the 1D density of states and, $v_{\mathrm{F}} \propto E^{1/2}$ while 1D DOS $\propto E^{-1/2}$, it is not a function of energy. Each transverse mode in this "electron waveguide" contributes the same conductance, $2 \times g_0$, where $g_0 = e^2/h = (25813\,\Omega)^{-1}$ is the quantum unit of conductance and the 2 accounts explicitly for spin. Thus, the conductance of a quantum point contact, $g = 2Ng_0$ is a measure of the number of 1D modes available or the width W of the channel in units of the Fermi wavelength:
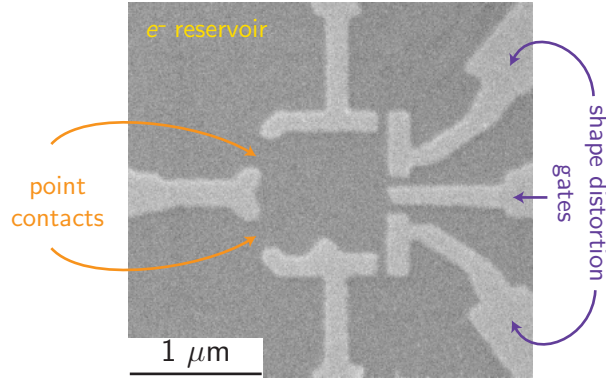
Figure 1.3: Micrograph of a typical quantum dot. Dark areas are the semiconductor surface; light areas are Au depletion gates.

$N = \mathrm{int}(2W/\lambda_\mathrm{F})$. The quantization of conductance in point contacts, seen in figure 1.4 was first observed by van Wees and coworkers [106] and Wharam and coworkers [107] in semiconductor 2DEGs whose long Fermi wavelength $\lambda_\mathrm{F} \approx 50\,\mathrm{nm}$ brings channels with small N within the range of microfabrication techniques.

Point contacts serve as the entrance and exit of a quantum dot, coupling it to the outside much as waveguides couple into and out of an optical cavity (figure 1.3). Their opening determine the dwell time τ_D or equivalently the escape rate γ_esc of electrons in a dot with chaotic classical dynamics

$$\gamma_\mathrm{esc} = \tau_D^{-1} = \frac{N\Delta}{\pi\hbar} \tag{1.1}$$

where

$$\Delta = \frac{2\pi\hbar^2}{m^* A} = \frac{7.14\,\mu\mathrm{eV}}{A/\mu\mathrm{m}^2} \tag{1.2}$$

is the mean single particle level spacing for a dot with area A.

In a dot with closed point contacts, $N < 1$, electrons tunnel into and out of the dot. If the capacitance of the dot C is sufficiently small, the energy required to add a single electron, e^2/C can be greater than $k_B T$ and the applied bias, blockading transport (figure 1.5a). In this Coulomb blockade regime, electrons can be added to the dot one by one by changing the chemical potential of the dot relative to the reservoirs. To add an electron, the chemical potential of the dot is lowered by changing the voltage on one of the gates
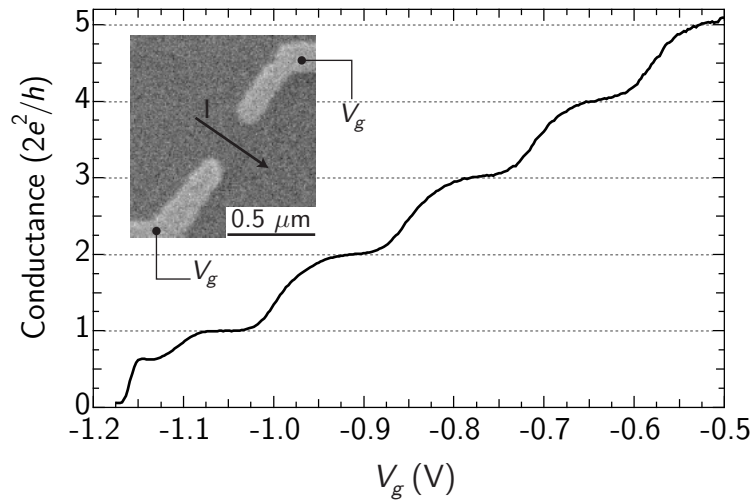
Figure 1.4: A constriction in the 2DEG creates a point contact with quantized transverse modes. The conductance of the point contact is quantized: $g = 2Ne^2/h$ where N is the number of transverse modes available in the point contact. (inset) Micrograph of a point contact. The number of modes is determined by the width of the construction which can be changed by varying the voltage applied to the depletion gates. These data were obtained in our lab by Sara Cronenwett and Joshua Folk.
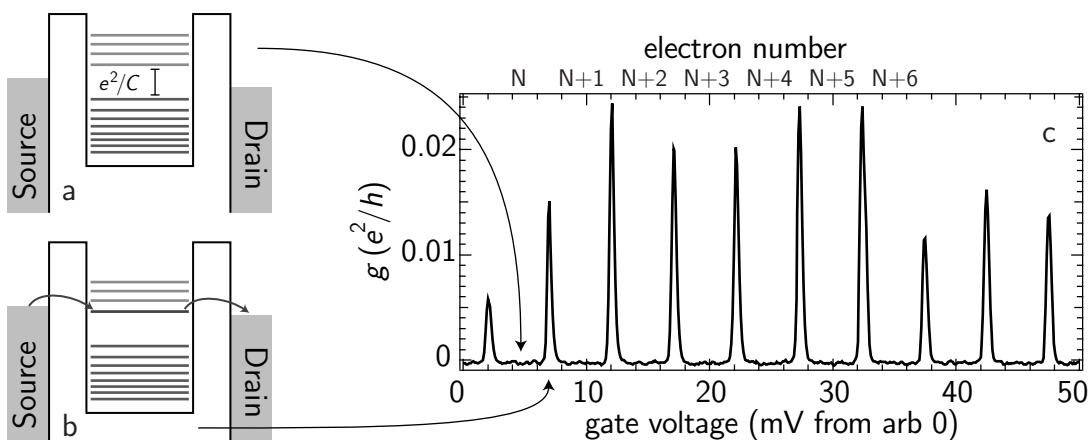
Figure 1.5: Schematic energy diagrams of a dot in Coulomb blockade showing the source and drain reservoirs (with a small bias voltage offsetting their Fermi levels), symmetric tunnel barriers, and the energy states confined in the dot. In (a), the capacitive energy gap e^2/C between the lowest unoccupied state and the highest occupied state in the dot prevents tunneling, blockading transport and fixing the number of electrons in the dot. In (b), the chemical potential of the dot has been lowered by changing the voltage on a shape distortion gate, aligning an energy state with the reservoirs, allowing electrons to tunnel through the dot one by one. The corresponding valleys (fixed electron number) and peaks (varying electron number) in conductance corresponding to these diagrams are illustrated in (c) with data from [39].

until the lowest unoccupied state (which is separated from the highest occupied state by the Coulomb gap e^2/C) lines up with the Fermi level of the source and drain reservoirs (figure 1.5b). At this point, electrons are free to tunnel into this unoccupied level from the source and tunnel out of it to the drain one by one resulting in a spike in the conductance of the dot (a small bias is applied to offset the Fermi levels in the source and drain). As the chemical potential of the dot is lowered still further, electrons can no longer tunnel out to the drain, returning the dot to blockade with its electron number increased by one.

The height of the conductance peaks seen in Coulomb blockade (figure 1.5) is governed by the tunneling rate of electrons into and out of the resonant energy states. The e^2/C gap only exists between the lowest unoccupied state and the highest occupied state. Thus, if the level spacing Δ is less than k_BT, the resonant tunneling occurs through many energy levels in the dot and the height of the peaks is essentially uniform. However, if $\Delta > k_BT$, the tunneling occurs through a single level (or a small number of levels) and the tunneling rate will vary from peak to peak as a function of the coupling of the dot wave function to those of the leads. The statistics of these fluctuations can be predicted [55], and measurements are in excellent agreement with the theory [26, 39].

There is a large literature focusing on closed mesoscopic systems and Coulomb blockade; for a recent review see [65]. The interesting case of a "half open" dot with one open and one closed point contact has also recently been investigated [30]. The experiments described in this dissertation were all conducted in "open" dots with symmetric point contacts each supporting one or more fully transmitting modes $N \geq 1$. In this regime, the discrete energy levels are broadened to a continuum by escape and Coulomb blockade is suppressed.

1.3.2 Universal Conductance Fluctuations (UCF)

One of the hallmarks of mesoscopic phenomena is random but repeatable fluctuations in measured quantities as external parameters are changed. In the regime of Coulomb blockade, the most obvious such fluctuation is in the height of the conductance peaks while in open systems, it is the random aperiodic fluctuations of conductance in response to small changes in magnetic field or the potential landscape (figure 1.6) [3, 69, 76]. While it is not possible to predict the conductance for a specific set of experimental parameters, the statistics of the fluctuations, including the full distribution of conductance probabilities, are *universal*, insensitive to details of system shape and size, provided that the classical dynamics are chaotic [49]. These universal conductance fluctuations (UCF) illustrate one
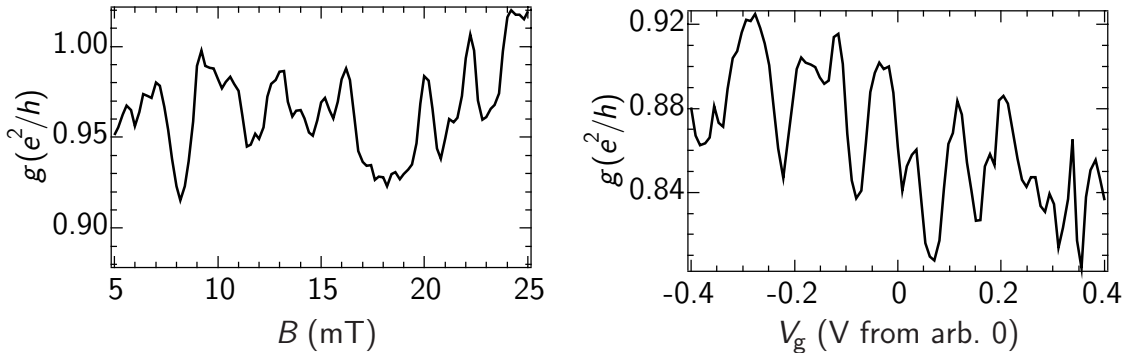
Figure 1.6: Small changes in external parameters such as magnetic field B or a shape distorting gate voltage V_g cause aperiodic repeatable fluctuations in the conductance of a quantum dot.

of the central themes in mesoscopic physics: while the details of an individual measurement are usually too complicated to predict, the statistical properties of an ensemble of measurements provide insight into the underlying physics.

The origin of the conductance fluctuations is easily understood for a two terminal device in the semiclassical approximation (see section 1.4.1). An electron enters the system and follows all possible Feynman paths inside the dot until it exits one of the leads. The conductance is determined by the probability of it returning to the entrance compared to the probability of exiting the opposite lead. These probabilities are in turn determined by a coherent sum over all the trajectories that exit a particular lead. Anything which changes the phase accumulated by these trajectories, such as a magnetic field or a change in path length due to shape distortion, will alter the interference pattern and change the conductance.

1.3.3   Weak Localization (WL)

While UCF are random and disappear when many measurements are averaged, the positive magnetoconductance seen in figure 1.7a in two individual measurements (gray traces) remains in an average of many measurements (black). This reduced conductance at zero magnetic field is the analog in quantum dots of weak localization (WL) in one and two dimensional systems. In the semiclassical model, this purely quantum mechanical effect is understood as enhanced backscattering. Each path that an electron can follow between
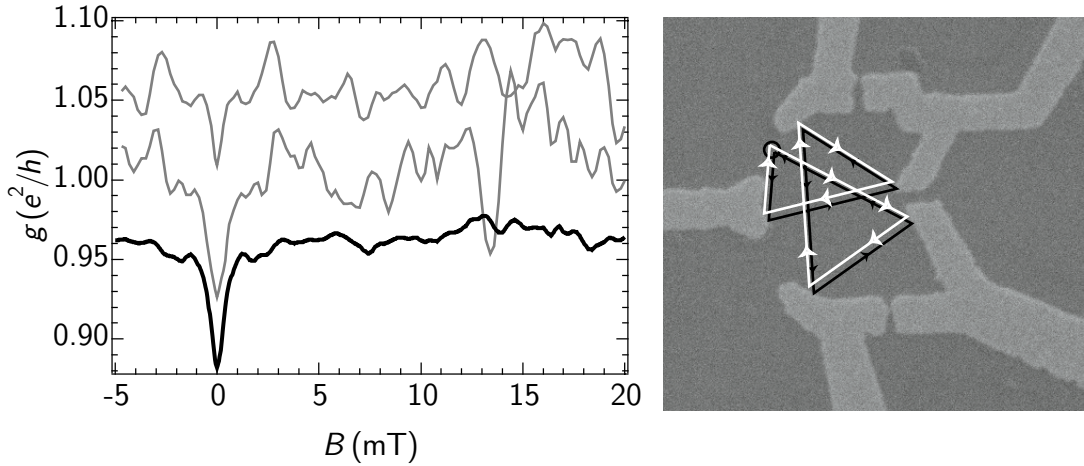
Figure 1.7: (left) Conductance is reduced at $B = 0$. The top two curves (offset for clarity) are individual magnetoconductance measurements showing UCF. The bottom curve is the average of many such measurements. Note that the UCF averages away while the reduced conductance at $B = 0$ remains. (right) The reduced conductance is a result of the constructive interference of time reversed trajectories at the origin. A magnetic field destroys this interference.

two points has a different length and passes through a different environment, imparting a different phase shift to the electron and leading to random interference at the destination. Each path which returns to the origin, however, has a time reversed twin which follows the same trajectory in reverse. These two paths have the same length and sample the same environment, accumulating the same phase shift. Each pair of time reversed paths interferes constructively at the origin, increasing the probability to find the electron there and reducing the conductance. The reduced conductance disappears in a magnetic field which breaks the time reversal symmetry (TRS); the Aharonov-Bohm phases accumulated by the former twins are opposite in sign, destroying the constructive interference and leaving the origin no different from any other point.

The shift in average conductance due to the breaking of time reversal symmetry is just one example of a second major theme in mesoscopic physics: changes in the symmetries of a system change the statistics of transport. Beyond the shift in $\langle g \rangle$, breaking TRS decreases the magnitude of the UCF (i.e. $\text{var} \, g_{B \neq 0} < \text{var} \, g_{B=0}$) [24] and the shape of the distribution of conductance probabilities [49]. Other changes in symmetry such as the introduction of a reflection symmetry [10] or the shift from a chaotic to an integrable shape [25, 76] can also

change the statistics of transport.

1.4   Theoretical frameworks

Predictions for quantum dot behavior in this dissertation are based on the two theoretical frameworks, semiclassical transport theory [7,31,97] and the theory of random matrices [14] discussed below. Although they start from very different premises, it is important to note that in appropriate limits, these two theories produce equivalent results.

1.4.1   Semiclassical transport

Semiclassical transport theory consists of studying the interference of electrons following classical paths through the system. Since it is essentially a classical theory with particle phase and interference added on, semiclassical models are useful for gaining an intuitive understanding of mesoscopic transport phenomena as in sections 1.3.2 and 1.3.3. Semiclassical theory can also provide quantitative statistical predictions about transport. Of particular interest here is the distribution of dwell times‡ for a chaotic dot with classical escape rate γ_{esc} (equation 1.1) [97]

$$P(t) \propto e^{-\gamma_{\mathrm{esc}}t} \tag{1.3}$$

for sufficiently long times. For shorter times, non-ergodic trajectories dominate and the probability distribution is specific to the exact shape of the dot with visible experimental consequences (figure 1.8b). During this time, the signed area traced out by a path accumulates diffusively , leading to a distribution of signed area [2,31]

$$P(A) \propto e^{-2\pi\alpha|A|} \tag{1.4}$$

where $\alpha = \sqrt{2\kappa N}$ is a characteristic inverse area and κ is a geometry dependent constant [1,74].

This distribution of areas is also the distribution of Aharonov-Bohm phases accumulated in a magnetic field which determines the effect of a magnetic field on transport. The power spectrum of UCF measured as a function of magnetic field can be calculated for

---

‡the probability that an electron remains in the dot for at least time t
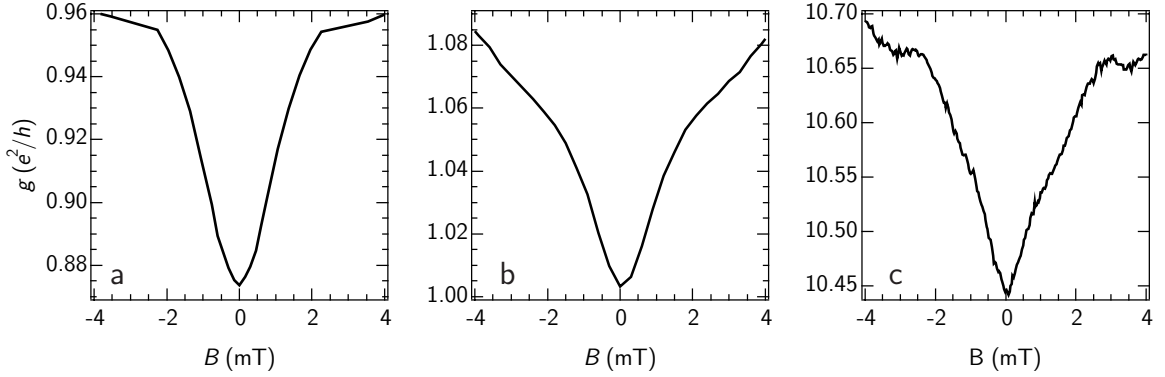
Figure 1.8: Magnetoconductance line shape around $B = 0$ for (a) chaotic (b) mixed, and (c) integrable device shapes. Note that in (b), the line shape transitions from Lorentzian (chaotic) to triangular (regular) around $2\,\mathrm{mT}$. Data for part c are taken from from [25].

$k_B T \gg \Delta$ [33, 53]

$$S(f) = S(0)e^{-2\pi B_c f} \tag{1.5}$$

where f is the frequency in cycles/T, $B_c = \alpha\varphi_0$ is the characteristic magnetic field, and $\varphi_0 = h/e = 4.14\,\mathrm{mT}\ \mu\mathrm{m}^2$ is the normal state quantum of magnetic flux. The distribution of areas also controls the sensitivity of the weak localization correction to magnetic field, yielding a Lorentzian line shape [10, 24, 25, 87]

$$\langle g(B)\rangle = \langle g\rangle_{B\neq 0} - \frac{\delta g}{1 + (2B/B_c)^2} \tag{1.6}$$

where $\delta g \equiv \langle g\rangle_{B\neq 0} - \langle g\rangle_{B=0}$ is the magnitude of the WL correction (see equation 1.13). Note that these exponential distributions are valid only for chaotic classical dynamics and either a regular shape [25, 76] or the persistence of non-ergotic trajectories will alter these statistics (see figure 1.8). This difference is illustrated in figure 1.8 which compares the Lorentzian WL line shape for a chaotic dot (1.8a) and the triangular line shape for a regular circular dot (1.8c)[§].The data in figure 1.8b has a Lorentzian line shape for small magnetic field which transitions to a triangular shape at slightly higher field. This indicates that the longer trajectories in the device are chaotic but that some short regular trajectories remain which can dominate the WL response at higher fields.
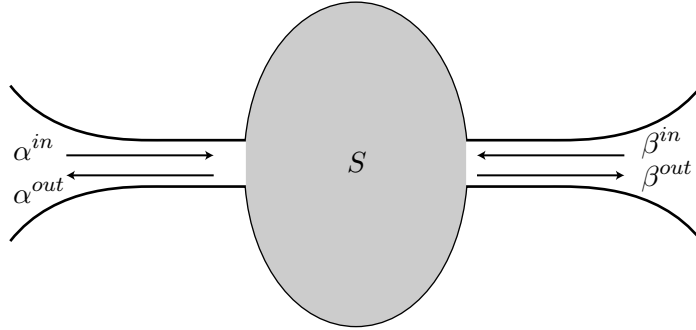
[§]Data from [25]

Figure 1.9: Random matrix theory reduces the quantum dot to a random scattering matrix S which couples incoming wave functions α^{in} and β^{in} to outgoing wave functions α^{out} and β^{out}.

1.4.2   Theory of Random Matrices (RMT)

One of the most successful theoretical approaches to mesoscopic systems has been through random matrix theory (RMT), a theory originally developed for modeling complex nuclear scattering. Many of the theoretical results needed for this work are derived through RMT however, an excellent recent review can be found in [14] so the discussion here will give only an overview of the calculation process.

Random matrix theory is attractive for complicated mesoscopic systems because it begins by discarding all of the system specific details and considering a black-box scattering region between two perfect electron waveguides. In the left (right) waveguide, the incoming electron wave function can be described in terms of complex coefficients α_n^{in} (β_n^{in}) which describe the magnitude and phase of the wave function in the N modes of each waveguide[¶]. For example, in a left waveguide with an infinite square well cross section, the incoming wave is

$$\psi^{\mathrm{in}} = \sum_{n=1}^{N} \alpha_n^{\mathrm{in}} \sin(ny) e^{ik_n x}. \tag{1.7}$$

We can then define the $2N \times 2N$ scattering matrix S

$$c^{\mathrm{out}} = S c^{\mathrm{in}} \tag{1.8}$$

[¶]All calculations and measurements in this dissertation are for symmetric leads with $N = N_{\mathrm{left}} = N_{\mathrm{right}}$ but some sources in the literature adopt the convention that $N = N_{\mathrm{left}} + N_{\mathrm{right}}$.

which transforms the incoming wave functions $c^{\text{in}} \equiv (\alpha_1^{\text{in}} \dots \alpha_N^{\text{in}}, \beta_1^{\text{in}} \dots \beta_N^{\text{in}})$ into the outgoing wave functions $c^{\text{out}} \equiv (\alpha_1^{\text{out}} \dots \alpha_N^{\text{out}}, \beta_1^{\text{out}} \dots \beta_N^{\text{out}})$. Thus S has the block form

$$S = \begin{pmatrix} r & t' \\ t & r' \end{pmatrix} \tag{1.9}$$

where r and r' are $N \times N$ matrices representing reflection from the left lead back to itself and from the right lead to itself and t and t' represent transmission from left to right and right to left, respectively. Because S is unitary, $tt^\dagger$, $t't'^\dagger$, $1 - rr^\dagger$, and $1 - r'r'^\dagger$ are all Hermitian matrices with the same set of eigenvalues, $\mathcal{T}_l$. These $\mathcal{T}_l$ are related to the conductance of the device g by the Landauer relation [36,68]

$$g = 2\frac{e^2}{h} \sum_{l=1}^{N} \mathcal{T}_l = 2\frac{e^2}{h} \sum_{p=1}^{N} \sum_{q=N+1}^{2N} |S_{pq}|^2 \,. \tag{1.10}$$

An ideal quantum point contact thus has all $\mathcal{T}_l = 1$.

For mesoscopic systems, the S matrix is chosen from an ensemble which represents the symmetries of the system. For chaotic quantum dots with open leads, S is uniformly distributed over the space of unitary matrices in the absence of time reversal symmetry ($B \neq 0$) and over the space of orthogonal matrices in the presence of time reversal symmetry ($B = 0$) [14]. This difference accounts for positive magnetoconductance (weak localization) described in section 1.3.3. The average element of S for the unitary case [14]

$$\left\langle |S|^2 \right\rangle = \frac{1}{2N} \qquad \text{no TRS} \tag{1.11}$$

differs from the average for the orthogonal case

$$\left\langle |S|^2 \right\rangle = \frac{1 + \delta_{pq}}{2N + 1} \qquad \text{TRS.} \tag{1.12}$$

Thus at $B = 0$, an electron is twice as likely to return to the mode where it started than to scatter to any other mode, consistent with the intuition of the semiclassical model. Combined with equation 1.10, this gives the WL correction

$$\delta g = N - \frac{2N^2}{2N + 1} = \frac{N}{2N + 1} \tag{1.13}$$

for g in units of g_0. Note that $\langle g \rangle_{B \neq 0}$ is just the series conductance of the two point contact leads. Other aspects of electron transport, for example the magnitude of the conductance fluctuations

$$\operatorname{var} g = \frac{N^2}{4N^2 - 1} \qquad\qquad B \neq 0 \qquad\qquad (1.14)$$

$$\operatorname{var} g = \frac{4N(N+1)^2}{(2N+1)^2(2N+3)} \qquad B = 0 \qquad\qquad (1.15)$$

again for g in units of g_0, can be calculated similarly [11].

Chapter 2

Phase Decoherence in Open Quantum Dots

Decoherence in the process by which the quantum mechanical properties of microscopic systems are transformed into the familiar classical behavior of macroscopic objects. Interactions between the system of interest and the "environment" (i.e. all parts of the universe which are not of interest) cause entanglement of their wave functions. Since the environment has many more degrees of freedom than the system, the information represented by the quantum mechanical correlations in the system diffuses into the environment and any attempt to measure the system yields only classical answers.

The time required for interaction with the environment to cause decoherence depends both on the strength of the system–environment coupling and on the size of the system, ranging from extremely long (the age of the universe or greater) for atoms and sub-atomic particles to unmeasurably short for macroscopic objects such as a cat. Mesoscopic systems fall between these extremes with decoherence times for electron phase on the order of 10^{-9} s. Because this is on the same order of magnitude as other important time scales in the dot such as the dwell time, the effects of decoherence can be measured in dc transport experiments, making mesoscopic systems ideal for the study of decoherence processes.

In addition to its importance as a basic physics problem, an understanding of decoherence is necessary for the development of technologies based on quantum mechanical effects. Chapter three explores the limitations that decoherence imposes on quantum dot sensors. Decoherence is also a limiting factor in the implementation of quantum computation [99], one proposed application of quantum dots which promises dramatically faster algorithms

for factoring large numbers [94], searching databases [45] and other problems which are difficult or time consuming for classical computers. Despite the development error correcting codes capable of preserving the fidelity of a quantum state in the face of decoherence, a threshold decoherence rate of 10^{-3}–10^{-4} per operation is required for arbitrary quantum computations [43]. The low temperature phase decoherence times measured in these experiments are on the order of $1\,\mathrm{ns}$ which would require an operation rate of at least $1\,\mathrm{THz}$. Hopefully a better understanding of decoherence will lead to more practical systems for quantum computation.

2.1   Theoretical treatment of decoherence

In order to model the effects of phase decoherence (dephasing) on mesoscopic transport, it must be incorporated into the theoretical framework. The first approach [22,77] is to model the dephasing as a fictitious voltage probe, a third lead equivalent to the two real leads except that it draws no net current (figure 2.1). As with the real leads, electrons scattering into this ϕ-lead have a random phase relationship with those emerging from it. The number of channels in the ϕ-lead γ_ϕ is set by the ratio of the dwell time τ_D to the dephasing time τ_ϕ

$$\gamma_\phi \equiv \frac{2\pi\hbar}{\tau_\phi \Delta} = 2N \frac{\tau_D}{\tau_\phi}. \tag{2.1}$$

This third lead is then incorporated into an S-matrix with dimension $2N + \gamma_\phi$. The difficulty with this model is that the dephasing is localized at the site of the ϕ-lead in contrast to the experimental reality of spatially uniform phase breaking. In addition, in order to create an S matrix, γ_ϕ is restricted to integer values while the dephasing time in a real system is a continuous parameter. This leads to some unphysical results such as the conclusion that the magnitude of the weak localization correction δg is the same for $\gamma_\phi = 1$ as for no dephasing [12,19]. A solution to these problems was proposed by Brouwer and Beenakker [20]. A tunnel barrier with transparency Γ_ϕ is introduced into a ϕ-lead with N_ϕ channels. In the limit $\Gamma_\phi \to 0$, $N_\phi \to \infty$ only the product $\gamma_\phi = N_\phi \Gamma_\phi$ is important. This cures both problems with the ϕ-lead model; γ_ϕ is a continuous parameter as it must be, and the large (infinite) width of the ϕ-lead removes the spatial localization of the dephasing.
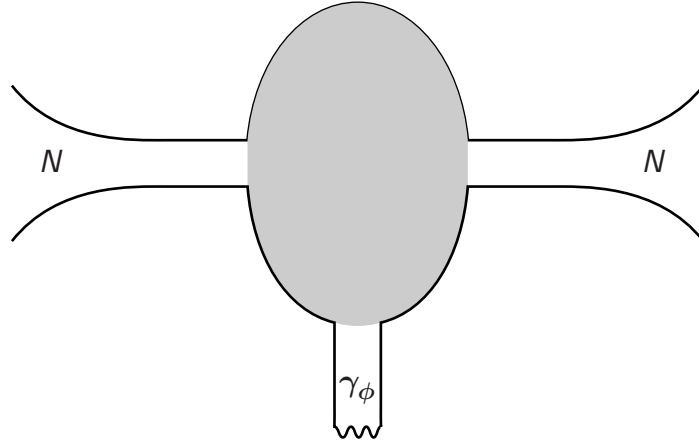
Figure 2.1: Decoherence is modeled as a fictitious extra lead with γ_ϕ modes attached to the dot. The "ϕ-lead" draws no current but electrons entering it have a random phase relationship with electrons leaving.

With these models, we can go on to examine the effect of dephasing on transport phenomena such as UCF and WL. Not surprisingly, the most obvious effect of dephasing is to reduce the strength of the quantum mechanical corrections to conductance. An exact expression for the size of the conductance fluctuations can be found for $N = 1$, $\gamma_\phi \gg 1$ [20], along with a more general approximate expression (for g in units of e^2/h) [12]

$$\operatorname{var} g \approx \frac{N^2}{\left(\sqrt{4N^2 - 1} + \gamma_\phi\right)^2} \qquad T = 0, B \neq 0 \qquad (2.2)$$

which reduces to equation 1.14 at $\gamma_\phi = 0$. A similar but more complicated expression is found for $B = 0$. Unfortunately, measurements of $\operatorname{var} g$ cannot be used directly to measure τ_ϕ because these expressions are valid only at $T = 0$. Since conductance is an explicit function of energy, a non-zero temperature reduces $\operatorname{var} g$ by making each measured value an average over a range of energies. The combination of implicit T dependence through τ_ϕ and explicit T dependence through thermal averaging complicates the picture and generally requires a numerical solution. See [49] for a full analysis.

The weak localization correction δg (equation 1.13) is also reduced by dephasing but,

as an average quantity, is unaffected by thermal averaging. In the localized ϕ lead model,

$$\delta g \approx \frac{N}{2N + \gamma_\phi},\qquad(2.3)$$

independent of temperature except through τ_ϕ (for g in units of e^2/h) [12]. The distributed ϕ-lead model [20] produces a complicated analytical expression for τ_ϕ which differs from equation 2.3 only for $N = 1$ and $\gamma_\phi \lesssim 10$ as seen in the inset to figure 2.5a. Because they can be and converted into a dephasing time with no free parameters, measurements of the magnitude of the weak localization correction is the standard method for determining τ_ϕ in 1D and 2D systems (see section 2.2.1). This chapter describes the first application of this technique to quantum dots.

Beyond reducing the magnitude of quantum corrections, dephasing has a second more subtle effect on mesoscopic transport. Dephasing cuts off the dwell time distribution (equation 1.3) at τ_ϕ since electrons which spend more time than this in the dot dephase. Thus the longest trajectories which accumulate the largest areas will not participate in interference, reducing the sensitivity of transport to magnetic field. This can be seen both in the power spectrum of the UCF and the width of the weak localization line shape (equations 1.5 and 1.6) as an increase in the characteristic magnetic field:

$$B_c = \varphi_0 \sqrt{\kappa(2N + \gamma_\phi)}.\qquad(2.4)$$

This effect does not depend explicitly on temperature and can be used to calculate τ_ϕ [28] but because of the geometric factor κ, it is significantly more cumbersome than determinations based on δg.

2.2   Causes of Dephasing

2.2.1   Diffusive One and Two Dimensional Conductors

Most studies of dephasing in mesoscopic systems have focused on disordered 1D and 2D conductors, where the dimensional crossover for quantum corrections to transport occurs when the sample width exceeds the phase coherence length $\ell_\phi = \sqrt{D\tau_\phi}$ ($D = v_\mathrm{F}^2 \tau_e/2$ is the diffusion constant for an elastic scattering time τ_e), effectively hiding the edges of the sample from coherent electrons [4]. For the interactions responsible for dephasing, the dimensional

crossover occurs when the sample width exceeds $\ell_T = \sqrt{D\hbar/k_B T}$ [51, 96]*.

At low temperature, electron-phonon scattering rates are small compared to electron-electron scattering rates[†] and, in the absence of magnetic impurities, two inelastic electron-electron scattering mechanisms dominate dephasing. The first consists of a strongly inelastic collisions with typical energy transfer on the order of the temperature. A single such collision is sufficient to dephase an electron (i.e. cause a phase shift on the order of 2π), causing dephasing with a rate $\tau_{ee}^{-1} \propto T^2$ [40, 42, 57, 86, 111]. In a 2DEG this rate is

$$\tau_{ee}^{-1} = \frac{\pi}{4} \frac{(k_B T)^2}{\hbar E_{\mathrm{F}}} \ln \frac{E_{\mathrm{F}}}{k_B T} \tag{2.5}$$

for $k_B T \ll E_{\mathrm{F}}$, the Fermi energy. The second mechanism, known as Nyquist phase breaking relies on low energy transfer quasi-elastic collisions. Nyquist dephasing is significant only at two dimensions or fewer and has a rate $\tau_{\phi N}^{-1} \propto T^{2/(4-d)}$ where d is the sample dimensionality [4]. In a *disordered* 2DEG, this rate is

$$\tau_{\phi N}^{-1} = \frac{k_B T}{2\pi\hbar} \frac{\lambda_F}{\ell_e} \ln \frac{\pi\ell_e}{\lambda_F}. \tag{2.6}$$

Because a sequence of these collisions is required to shift the phase by 2π, Nyquist dephasing is not an exponential process whose rate can simply be added to τ_{ee}^{-1}; the sequence of collisions can be destroyed by a single large energy transfer collision. See references [4, 32, 71] for further discussion. In the following, however, we approximate the total dephasing rate due to electron-electron scattering as sum of these rates, $\tau_{\phi}^{-1} \approx \tau_{\phi N}^{-1} + \tau_{ee}^{-1}$ [27, 67, 91].

Measurements of $\tau_{\phi}(T)$ in disordered 2D and 1D semiconductors [27, 67, 91] and 1D metals [32, 71] based on weak localization find good agreement with these theoretical results down to $\sim 0.1\,\mathrm{K}$, well below the temperatures in this experiment. At lower temperatures, dephasing appears to saturate in a variety of systems, including quantum dots [17, 28, 49, 81]. Many theoretical explanations have been proposed but as of this writing, the issue remains unsettled [5, 60, 80].

---

*The corresponding values for ballistic transport are $\ell_\phi = v_{\mathrm{F}} \tau_\phi$ and $\ell_T = v_{\mathrm{F}} \hbar / k_B T$.

[†]$\tau_{e-\mathrm{ph}}^{-1}(T) \propto T^3$ in GaAs/AlGaAs 2DEGs and is lower than τ_ϕ^{-1} by an order of magnitude over the entire temperature range studied. See [79].

2.2.2   Ballistic Conductors and Quantum Dots

Since by definition there is no backscattering and thus no weak localization in ballistic conductors, more experimentally involved methods such as a double slit experiment [109] or tunneling between parallel 2DEGs [83] must be employed to measure dephasing. These experiments find that the Nyquist contribution to dephasing is not significant in ballistic systems and that $\tau_\phi \approx \tau_{ee}$ in good agreement with equation 2.5 [83, 109, 110]. Although there is no detailed theoretical support, it appears that $\tau_\phi \propto T^{-2}$ in ballistic systems.

In closed 0D systems, a series of experiments on dots embedded in Aharonov-Bohm rings [108] suggest that some phase coherence is retained up to 3 ns at 100 mK. However, these experiments made no attempt to determine τ_ϕ exactly or to study it as a function of temperature. Experiments attempting to determine τ_ϕ from the difference in the average height of Coulomb Blockade peaks at $B = 0$ and $B \neq 0$ are ongoing [38, 39]. Theoretical studies [51, 95] predict that τ_ϕ is also proportional to T^{-2} in closed dots for the intermediate temperature range explored in this experiment, $\ell_T > L$ but $k_B T \gg \Delta$. To our knowledge, there has been no theoretical discussion of τ_ϕ in open quantum dots.

2.3   Measurements

Here, we describe the first use of the weak localization correction δg to measure the dephasing time in open quantum dots. In ballistic dots with areas ranging from 0.4 to $4\,\mu\mathrm{m}^2$ and single channel point contact leads ($N = 1$), we find that τ_ϕ shows behavior similar to that seen in disordered 2D conductors including contributions from both large energy and Nyquist scattering processes. These conclusions are verified by comparison to $\tau_\phi(T)$ measured with three other techniques in the same dots.

Measurements on four quantum dots (figure 2.2) with lithographic areas of 0.4 (2 dots), 1.9, and $4.0\,\mu\mathrm{m}^2$ ($\Delta = 17.9$, 3.8, and $1.8\,\mu\mathrm{eV}$ respectively) are reported. The elastic mean free path in the 2DEG measured with all gates grounded is $\sim 6\,\mu\mathrm{m}$, larger than all device sizes, assuring ballistic transport within the dots. This particular 2DEG (see appendix B), grown by Ken Kampman at UCSB was exceptional. Perhaps due to its 160 nm depth below the surface, it formed clean smooth point contacts with low noise, greatly facilitating this experiment. The dots were measured in a ^{3}He cryostat at temperatures ranging from 330 mK to 4 K using standard 4-wire lock-in techniques at ~ 100 Hz. The bias current, $I_{\mathrm{bias}} = 0.5\,\mathrm{nA}$, was small enough not to cause heating as verified by identical results for
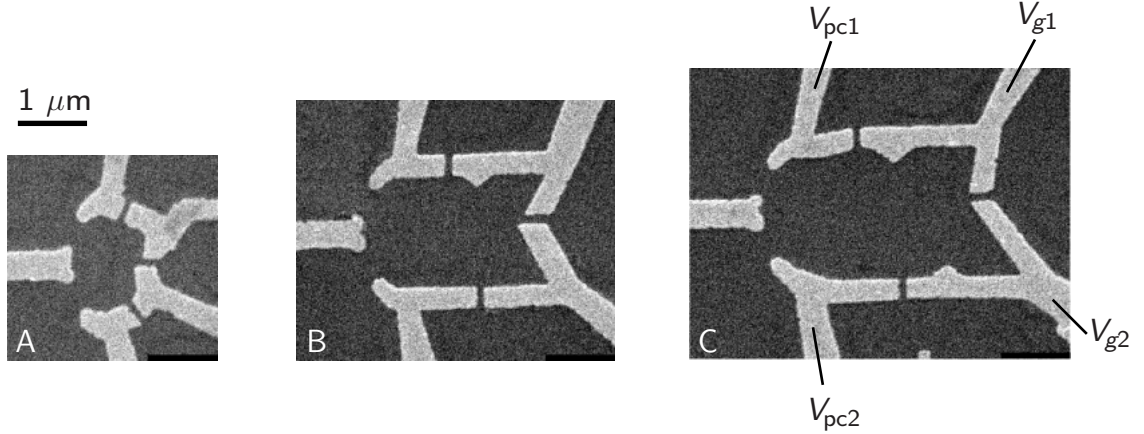
Figure 2.2: Electron micrographs of the $0.4\,\mu\text{m}^2$ (a), $1.9\,\mu\text{m}^2$ (b), and $4.0\,\mu\text{m}^2$ (c) devices used in this experiment. Dot (c) has labels denoting the voltages applied to specific depletion gates.

$I_\text{bias} = 0.5$ and $1.0\,\text{nA}$.

At these temperatures, weak localization and UCF are comparable in magnitude as seen in the colored traces of figure 2.4. By measuring an ensemble of device shapes created by changes in the shape distorting gate voltages V_{g1} and V_{g2}, the UCF can be averaged away, leaving only the weak localization correction. The measurement procedure is illustrated in figure 2.3. First, the range of V_{g1} and V_{g2} to be measured is established. Then V_pc1 and V_pc2 are swept in a raster to find the plateau with $N = 1$ channel in each point contact. Since changes in the gate voltages have a small but significant electrostatic effect on the point contacts, this sweep is repeated at each of the four corners of the (V_{g1}, V_{g2}) range. The shape of the dot can then be distorted with V_{g1} and V_{g2} while the leads are maintained at one channel by adjusting V_pc1 and V_pc2 to settings interpolated from the values found at the corners. Magnetoconductance measurements are made at the 47 values of V_{g1} and V_{g2} indicated by blue points on the conductance landscape in figure 2.3. Figure 2.4 shows $g(B)$ at four of these points along with the average $\langle g(B) \rangle$ of all 47.

Figure 2.5a shows δg at $N = 1$ as a function of temperature for the four devices. Using $\gamma_\phi(\delta g)$ from ref. [20], each point in figure 2.5a is converted to γ_ϕ and then, using equation 2.1, to τ_ϕ. The resulting $\tau_\phi(T)$ is shown in figure 2.5b. While dots with different areas have different values of δg, τ_ϕ appears to be independent of dot area. The apparent high temperature roll-off of τ_ϕ seen for the larger devices results from a breakdown of the model
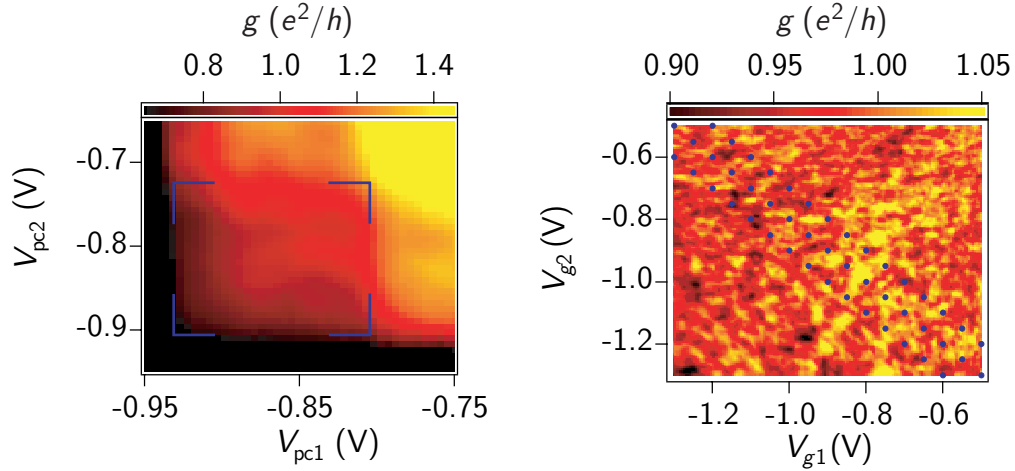
Figure 2.3: (left) Conductance as a function of V_{pc1} and V_{pc2} with the $N = 1$ plateau bracketed in blue. (right) Conductance as a function of V_{g1} and V_{g2} with blue circles marking the 47 points at which magnetoconductance was measured.
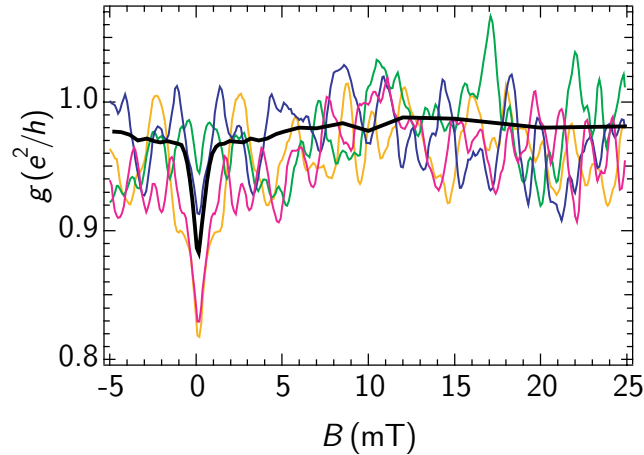

Figure 2.4: Single magnetoconductance measurements (colored curves) show UCF and weak localization with approximately equal magnitude. An average over 47 of these traces (black) reduces the UCF giving the average weak localization correction.

in [20] when ℓ_ϕ is on the order of the dot size; a few short non-ergodic trajectories, not accounted for in [20], dominate coherent backscattering (see figure 1.8 and accompanying discussion).

As seen in figure 2.5b, the temperature dependence of τ_ϕ falls between $\tau_\phi \propto T^{-2}$ and $\tau_\phi \propto T^{-1}$ and is well fit by the sum of the large energy transfer and Nyquist dephasing rates for *diffusive 2D systems*, equations 2.5 and 2.6. Choosing an effective value of $\ell_e = 0.25\,\mu$m gives

$$\tau_\phi^{-1} = 12.8T + 1.4T^2 \ln \frac{74.3}{T} \tag{2.7}$$

for T in K and τ_ϕ in ns, the solid line in figure 2.5. We do not know if this value of ℓ_e corresponds to any physical length in the problem; certainly it is much shorter than the ℓ_e of the unconfined electron gas. This temperature dependence is somewhat surprising since both 2D ballistic systems and 0D closed dots are predicted to have $\tau_\phi \propto T^{-2}$ (see section 2.2.2). We note that, while $\tau_\phi(T)$ does not show a low temperature saturation in the temperature range measured, subsequent measurements show some saturation below $100\,$mK and a $\tau_\phi(T)$ consistent with the present data above $100\,$mK [49].

To check the results based on weak localization amplitude at $N = 1$, we compare to three other measurements of τ_ϕ in the same devices. The first comparison is to τ_ϕ obtained from weak localization amplitude at $N = 2$, $\delta g_{N=2}$, measured just as for $N = 1$ and using equations 2.1 and 2.3 to convert from $\delta g_{N=2}$ to τ_ϕ. With no adjustable parameters, the $\delta g_{N=1}$ and $\delta g_{N=2}$ results are consistent within experimental errors as shown in figure 2.6 for the 0.4 and $4.0\,\mu$m^2 dots.

The second comparison is to τ_ϕ extracted from the power spectra of UCF as described in [28] and in equations 1.5 and 2.4. Figure 2.7 shows power spectra of $g(B)$ for the $4.0\,\mu$m^2 dot which are consistent with equation 1.5 over three orders of magnitude, and a two parameter ($S(0)$ and B_c) fit to the power spectrum at each temperature gives $B_c(T)$. The dephasing time is then determined by equation 2.4 with κ chosen to give a best fit with the $\delta g_{N=1}$ data. Figure 2.7 shows good agreement between the two methods over the whole temperature range.

The final comparison is to τ_ϕ extracted from the line shape of the weak localization correction around $B = 0$ (equation 1.6). Figure 2.8 shows shape averaged $\langle g(B) \rangle$ for the $4.0\,\mu$m^2 dot along with two parameter (δg and B_c) fits to equation 1.6. Values for τ_ϕ are
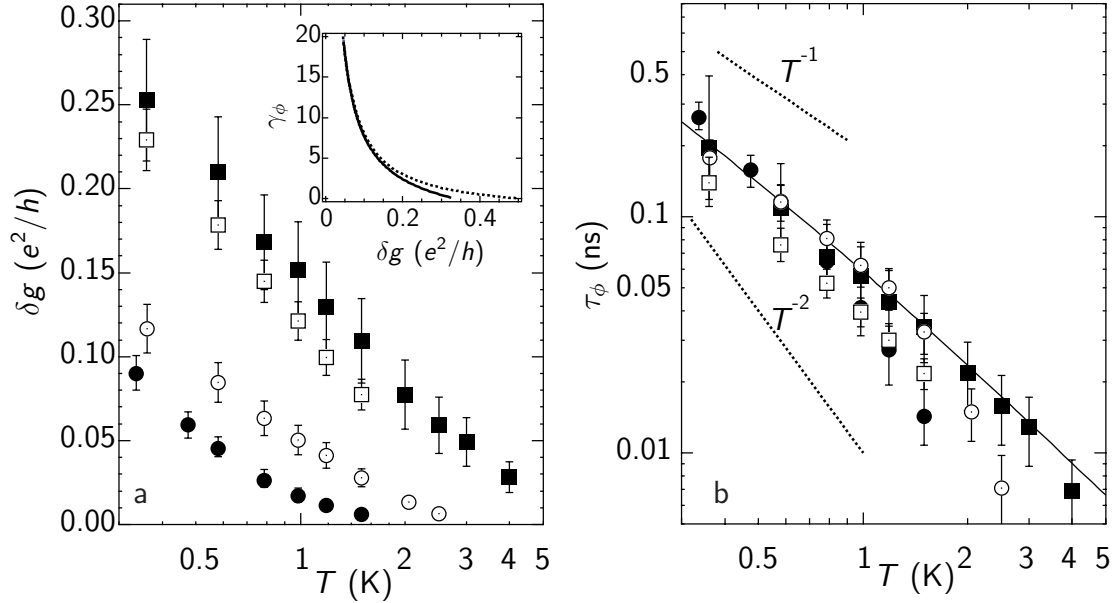
Figure 2.5: (a) Shape averaged weak localization δg as a function of temperature for the four measured devices: $0.4\,\mu\text{m}^2$ (■, □), $1.9\,\mu\text{m}^2$ (○), and $4.0\,\mu\text{m}^2$ (●). Error bars reflect uncertainty in δg as a result of conductance fluctuations remaining due to limited ensemble size. Inset: Comparison of phase breaking rate $\gamma_\phi(\delta g)$ at $N = 1$ using the ϕ-lead model (equation 2.3, dashed line) [12] and the distributed ϕ-lead model of [20]. (b) Phase coherence time τ_ϕ determined from δg at left. The dotted lines show $\tau_\phi \propto T^{-1}$ and T^{-2} as guides to the eye. The solid line shows $\tau_\phi^{-1} = \tau_{ee}^{-1} + \tau_{\phi N}^{-1}$ for a disordered system with $\ell_e = 0.25\,\mu\text{m}$ (equation 2.7).
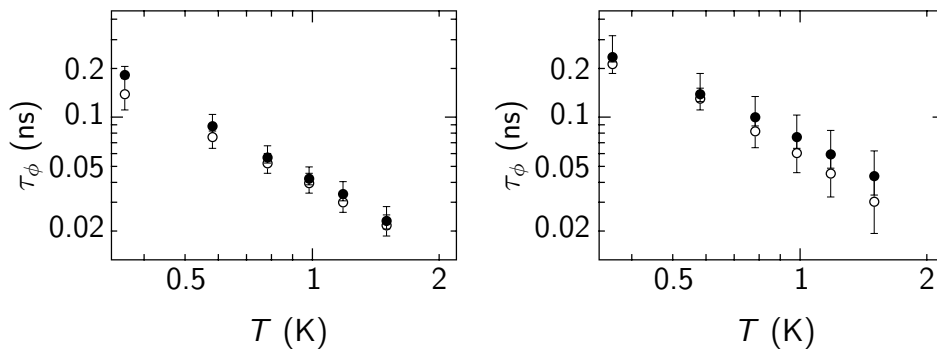

Figure 2.6: Comparison of τ_ϕ extracted from weak localization amplitude at $N = 1$ (○) and $N = 2$ (●) for the $0.4\,\mu\text{m}^2$ (left) and $4.0\,\mu\text{m}^2$ (right) dots.
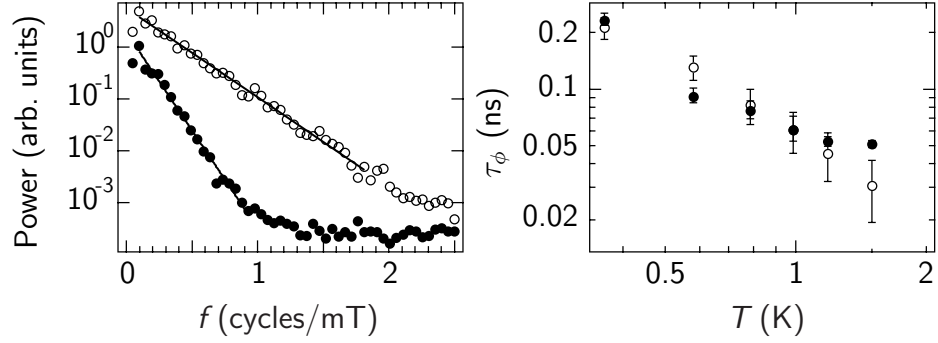
Figure 2.7: (left) Fit of equation 1.5 to power spectral density of the UCF at $N = 1$ for $T = 360\,\text{mK}$ (○) and $T = 1\,\text{K}$ (●). (right) Comparison of τ_ϕ extracted from the UCF power spectra (●) and from the weak localization correction at $N = 1$ (○) for the $4.0\,\mu\text{m}^2$ dot.
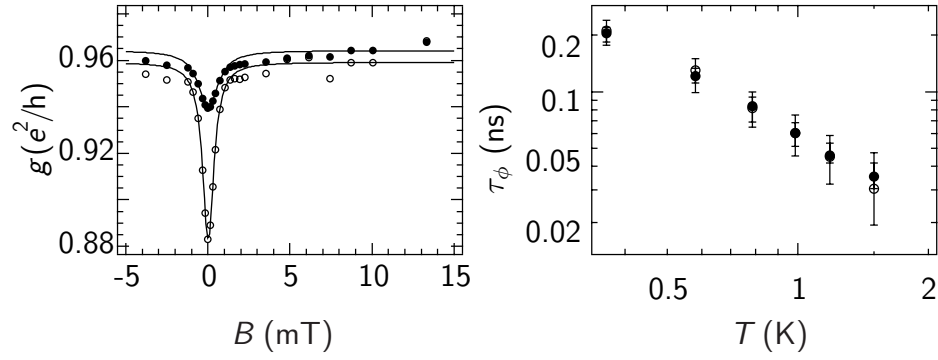

Figure 2.8: (left) Fit of equation 1.6 to average weak localization lineshape at $N = 1$ for the $4.0\,\mu\text{m}^2$ dot for $T = 360\,\text{mK}$ (○) and $T = 1\,\text{K}$ (●). . (right) Comparison of τ_ϕ extracted from the width of the fit (●) and from weak localization amplitude (○).

extracted from B_c using equation 2.4 with κ chosen to give a best fit to the $\delta g_{N=1}$ results. Again, the two methods agree within experimental error.

The good agreement of τ_ϕ over four measurement techniques with different theoretical supports (RMT versus semiclassical theory) gives us confidence in the measurements and their interpretation. The method based on δg is clearly preferred for the same reasons it is the standard in 1D and 2D systems: it is the easiest experimentally and it relates a measured quantity, δg, to τ_ϕ with no adjustable parameters.

Chapter 3

High Bias Transport

Beyond the intrinsic physical interest in decoherence, electron dephasing limits the performance of technological devices based on mesoscopic systems. The restrictions which decoherence places on quantum computing are discussed briefly in the previous chapter. This chapter focuses on quantum dots as sensors and in particular on the quantum dot magnetometer.

Most experiments in quantum dots are performed at low bias, typically $\lesssim 20\,\mu\text{V}$ for open dots. This is not ideal for technological applications; many will require higher bias to produce easily measurable signals. In the tunneling regime, $g \ll e^2/h$, experiments have exploited the non-linear conduction of quantum dots at higher bias to perform energy level spectroscopy [56,100]. In open dots, the conduction remains essentially linear at high bias, and the experiments presented in this chapter demonstrate that the primary effect of the increased bias is to heat the electrons. Transport is characterized by an effective temperature derived from Joule heating at the point contacts and Wiedemann-Franz out diffusion of thermal electrons. In a quantum dot device, the optimum operating bias is a balance between increased signal from high bias and loss of quantum interference and increased noise from elevated electron temperature. With the effective temperature model, we analyze a quantum dot magnetometer, investigating optimal design parameters and performance possibilities, and comparing it to alternative technologies for micron scale magnetometry.
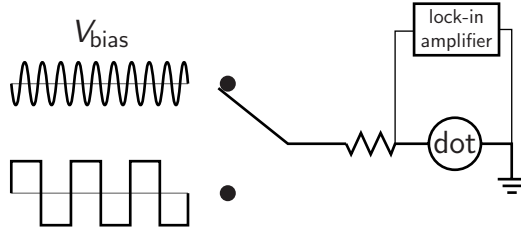
Figure 3.1: Schematic of the dot and measurement circuit showing the two configurations used to measure conductance at low bias (upper) and high bias (lower). The high bias configuration uses a square wave excitation in order to measure conductance at a single value of bias.

3.1   Measurements

To understand the effect of bias on transport, unaveraged magnetoconductance measurements $g(B) = I_{\mathrm{bias}}/V$ made at low rms current bias I_{bias} for various values of the cryostat temperature T_0 were compared to similar measurements made at elevated I_{bias} and low cryostat temperature. All measurements were carried out in a ^{3}He cryostat on the $4.0\,\mu\mathrm{m}^2$ device described in the previous chapter (see figure 2.2c for a micrograph). Two different measurement configurations (figure 3.1) were used. In the first configuration, identical to that used in the previous chapter, conductance was measured for several cryostat temperatures between $340\,\mathrm{mK}$ and $1.5\,\mathrm{K}$ using standard current biased lock-in techniques with I_{bias} fixed at $0.5\,\mathrm{nA}$. In the second configuration, T_0 was fixed and conductance was measured for several values of I_{bias} using lock-in detection of a square wave excitation.

Magnetoconductance measurements made in both configurations are shown in figure 3.2. The close agreement of even the fine features of measurements made in these two configurations allows us to describe the effect of increased bias with a phenomenological *effective temperature* T_{eff} shown in figure 3.3 for $T_0 = 340$ and $540\,\mathrm{mK}$. Over most of the experimental range, this effective temperature can be interpreted as the electron temperature in the dot since electrons in the dot are in thermal equilibrium. Energetic electrons entering the dot thermalize primarily by inelastic electron-electron collisions whose rate τ_{ee}^{-1} (equation 2.5) is at least comparable to the escape rate of electrons from the dot τ_D^{-1} (equation 1.1). For this dot with $E_{\mathrm{F}} = 6.4\,\mathrm{meV}$, $N = 1$, and $\Delta = 1.8\,\mu\mathrm{eV}$, the dwell time is $\tau_D = 1.2\,\mathrm{ns}$. At $340\,\mathrm{mK}$, $\tau_{ee} = 1.2\,\mathrm{ns}$ which is comparable to τ_D and with increasing temperature, τ_{ee}
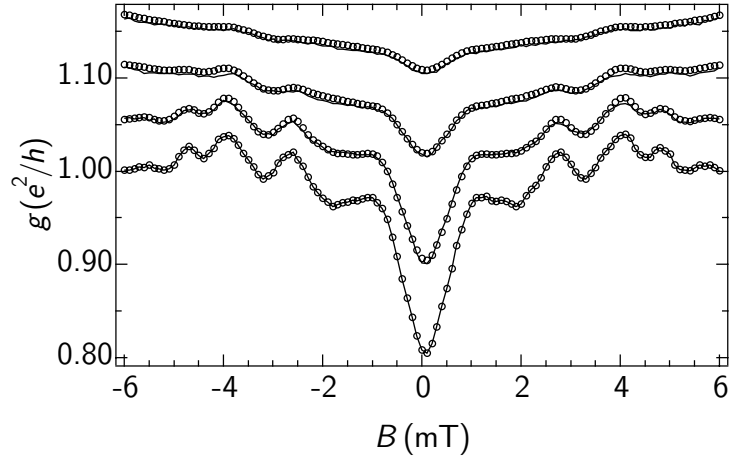
Figure 3.2: Measured magnetoconductance $g(B)$. Solid lines correspond to $g(B)$ at $I_{\text{bias}} = 0.5\,\text{nA}$ for $T_0 = 340, 410, 680,$ and $990\,\text{mK}$ (bottom to top) while open circles show $g(B)$ at $T_0 = 340\,\text{mK}$ for $I_{\text{bias}} = 0.5, 3, 7,$ and $12\,\text{nA}$ (bottom to top). Each pair of curves has been offset for clarity.

decreases further, $\tau_{ee} = 0.17\,\text{ns}$ at $T = 1\,\text{K}$, allowing electrons to come into thermal equilibrium within the dot. This is in contrast to recent experiments which found an effective temperature $T_{\text{eff}} = eV/k_B$ for electrons out of thermal equilibrium ($\tau_D < \tau_{ee}$), much higher than we find for thermalized electrons (equation 3.3)* [72].

The measured effective temperature can be quantitatively modeled as a balance of energy added to the dot by high bias electrons with the energy lost to the environment. The power input is the Joule heating from the point contacts, $P_{\text{total}} = I_{\text{bias}}^2/g$. This heating occurs not in the 1D channel of the point contact itself but at the ends where it widens into the dot and the reservoir. Thus the heat generated is divided, not necessarily evenly, between the dot and the reservoir [46,92]; as discussed below, our data are best fit assuming ~10% asymmetry in heating. The dominant cooling mechanism is the diffusion of warm electrons out of the dot, as described by the Wiedemann-Franz relation [8]. Although originally developed for classical, diffusive metal systems, the Wiedemann-Franz relation is remarkably robust having been both predicted [44,90] and measured (to within a factor of 2) [82] to apply to ballistic point contacts. For the geometry of a quantum dot with two electrical resistances in series and two thermal resistances in parallel, the Wiedemann-Franz

---

*For $T_{\text{eff}} \gg T_0$, the effective temperature derived from equation 3.3 is about $0.2eV/k_B$.
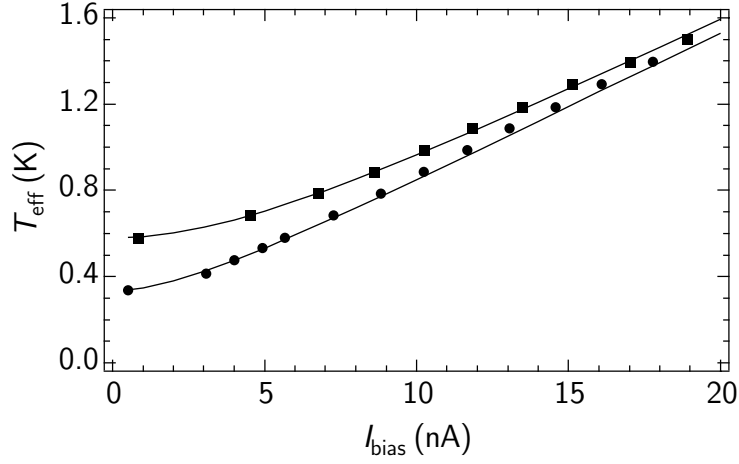
Figure 3.3: Measured effective temperature as a function of I_{bias} for $T_0 = 340\,\text{mK}$ (●) and $580\,\text{mK}$ (■) along with the values predicted by equation 3.3 with $P_{\text{dot}} = 0.4\,I_{\text{bias}}^2/g$ (solid lines).

relation gives a thermal conductivity

$$\sigma_{\text{th}} = 4gTL_0 \tag{3.1}$$

with the Lorenz number

$$L_0 = \left(\frac{k_B}{e}\right)^2 \frac{\pi^2}{3}. \tag{3.2}$$

Assuming that the reservoirs are in good thermal contact with the cryostat and remain at T_0, this yields an effective temperature

$$T_{\text{eff}}^2 = T_0^2 + \frac{P_{\text{dot}}}{2gL_0} \tag{3.3}$$

where P_{dot} is the power heating the dot. For a symmetric point contact, P_{dot} is half of the total Joule power but we find best agreement with our data for $P_{\text{dot}} = 0.4P_{\text{total}}$ (figure 3.3). Presumably, this deviation from $1/2$ is due to asymmetry in the point contacts [46, 92]. Cooling via the substrate is neglected since the electron-phonon interaction time at the temperatures studied here is longer than τ_D [78].
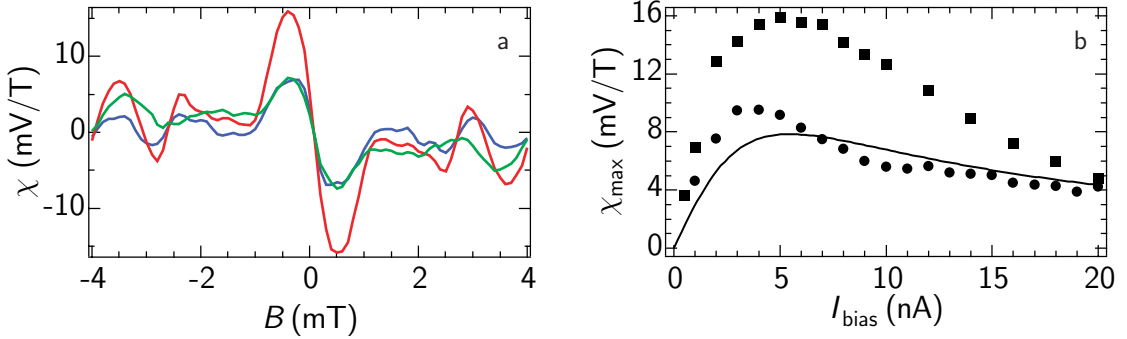
Figure 3.4: (a) The voltage response $\chi(B)$ (equation 3.4) measured at $I_{\text{bias}} = 1\,\text{nA}$ (blue), $5\,\text{nA}$ (red), and $16\,\text{nA}$ (green). At $1\,\text{nA}$, the signal is small due to low bias while at $16\,\text{nA}$, heating reduces conductance fluctuations. χ is largest at an intermediate bias. (b) The maximum of the voltage response χ_{max} as a function of bias current. Solid symbols represent measurements for two different configurations of the shape distortion gates. The theoretical ensemble average value (solid line) differs from the single measurements due to conductance fluctuations.

3.2 Quantum Dot Magnetometer

The effective temperature model along with the many characteristics of transport known from low bias measurements allow us to examine the performance of quantum dots as sensors and to optimize the operating conditions for a given task. As an example, we will analyze the performance of a quantum dot magnetometer which takes advantage of the large magnetoconductance of quantum dots around $B = 0$ (see section 1.3.3) to measure absolute magnetic field with spatial resolution on the order of the size of the dot.

If noise is independent of bias, as in the case of the measured dot, the optimum operating parameters are determined by maximizing the voltage response

$$\chi \equiv \frac{dV}{dB} = -\frac{I_{\text{bias}}}{g^2}\frac{dg}{dB}. \tag{3.4}$$

This response is 0 at $B = 0$ since there is a minimum in conductance but is maximum at a small magnetic field B_{max} as seen in figure 3.4a. Two measurements of $\chi_{\text{max}} \equiv \chi(B_{\text{max}})$ for different values of the shape distorting gate voltages are shown in figure 3.4b. While conductance fluctuations cause χ_{max} to vary for any individual measurement, the ensemble averaged response can be calculated for a chaotically shaped ballistic dot from the

Lorentzian line shape of the weak localization [10] (see section 1.4.1)

$$\langle g(B) \rangle = \langle g \rangle_{B \neq 0} - \frac{\delta g}{1 + (2B/B_c)^2}. \tag{3.5}$$

whose height δg and width B_c both depend on temperature through dephasing as seen in equations 2.3 and 2.4 respectively. The maximum voltage response thus occurs at

$$B_{\mathrm{max}} = \frac{B_c}{2\sqrt{3}} \sqrt{1 - \frac{\delta g}{\langle g \rangle}}. \tag{3.6}$$

which in turn gives

$$\chi_{\mathrm{max}} = \frac{3\sqrt{3}\, \delta g I_{\mathrm{bias}}}{4 B_c \sqrt{\langle g \rangle} (\langle g \rangle - \delta g)^{3/2}} \tag{3.7}$$

Using equation 3.7, along with the dephasing times measured in the previous chapter (equation 2.7) and the effective temperature of equation 3.3 yields the theoretical average voltage response $\langle \chi_{\mathrm{max}} \rangle$ shown as the solid line in figure 3.4. The measured values are not ensemble averaged and thus differ from the calculated value due to conductance fluctuations. While this requires recalibration of the sensor for each value of the shape distorting gate voltages and for each thermal cycle, the UCF can be used to improve the response of the magnetometer by as much as a factor of two by "tuning" the dot to a configuration with high χ_{max}. In addition, since transport is symmetric in magnetic field, $B = 0$ is indicated unambiguously. These results can be used to design devices specifically for magnetometry. The highest value of χ_{max} for a given T_0 and dot area is shown in figure 3.5a. The operating current required for this most sensitive operation at $T_0 = 300\,\mathrm{mK}$ is shown in figure 3.5b. Note that the optimum dot size shifts slightly with temperature.

If external noise is minimized, the fundamental limit on performance is the voltage noise of the dot itself. Dot noise is a combination of shot and Johnson-Nyquist noise which add to give a total noise [66]
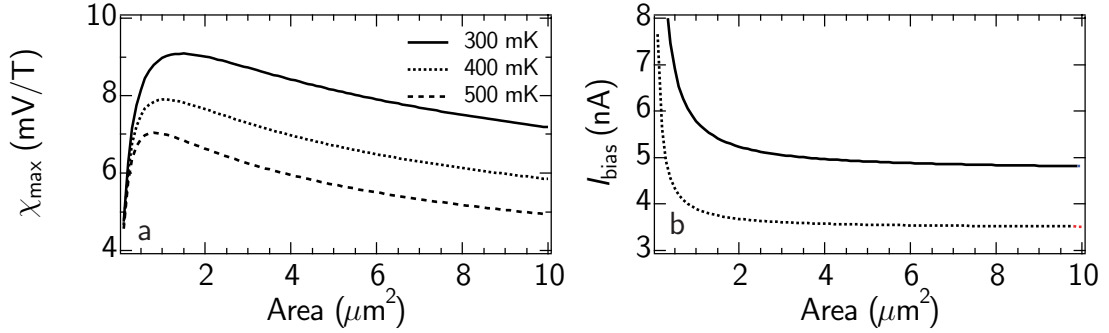
$$S_V^{1/2} = \sqrt{4 k_B T^* / g} \tag{3.8}$$

Figure 3.5: (a) Calculated average χ_{max} as a function of dot area. Note that the optimum dot area changes slightly with operating temperature. (b) Operating bias for optimum χ_{max} (solid) and lowest noise (dashed) operation.

with equivalent noise temperature

$$T^* = T \left[1 + \alpha \left(\frac{eI_{\text{bias}}}{2gk_BT} \coth \frac{eI_{\text{bias}}}{2gk_BT} - 1 \right) \right]. \tag{3.9}$$

Here $\alpha = 1/4$ is the suppression factor for shot noise in quantum dots compared to the poissonian value $S_I^{\text{dot}} = 1/4 S_I^{\text{classical}} = 1/4(2eI)$ [54]. This noise can be combined with the voltage response calculated above to give $S_B^{1/2} = S_V^{1/2}/\chi$ shown in figure 3.6a. The noise in the device measured is far above this limit, $S_V^{1/2} \sim 150\,\text{nV}/\sqrt{\text{Hz}}$ which translates to $S_B^{1/2} \sim 10\,\mu\text{T}/\sqrt{\text{Hz}}$. This noise could be greatly reduced by measuring at a frequency above the $1/f$ knee. See for example [66] where the authors have measured a point contact with a $1/f$ knee below $1000\,\text{Hz}$.

Quantum dots compare reasonably well with other technologies for micron scale absolute magnetometry. While noise prevents the dot measured here from being a competitive magnetometer, an optimized $1\,\mu\text{m}^2$ dot could have *average* field noise $S_B^{1/2} \sim 100\,\text{nT}/\sqrt{\text{Hz}}$ at $300\,\text{mK}$ (figure 3.6a). As explained above, this noise can be reduced by a factor of two by tuning the shape distortion gates for maximum voltage response. This compares well to $\sim 200\,\text{nT}/\sqrt{\text{Hz}}$ for a submicron ballistic Hall probe [41]. Both quantum dots and hall bars have an order of magnitude higher noise than a state of the art commercial SQUID, $\sim 6\,\text{nT}/\sqrt{\text{Hz}}$ for a $1\,\mu\text{m}^2$ device [29]. Note however that the ultimate size limit for SQUIDs is the magnetic penetration length ($\sim 85\,\text{nm}$ in Nb) whereas for devices based on chaotic quantum interference, the ultimate size limit is the Fermi wavelength which can be orders
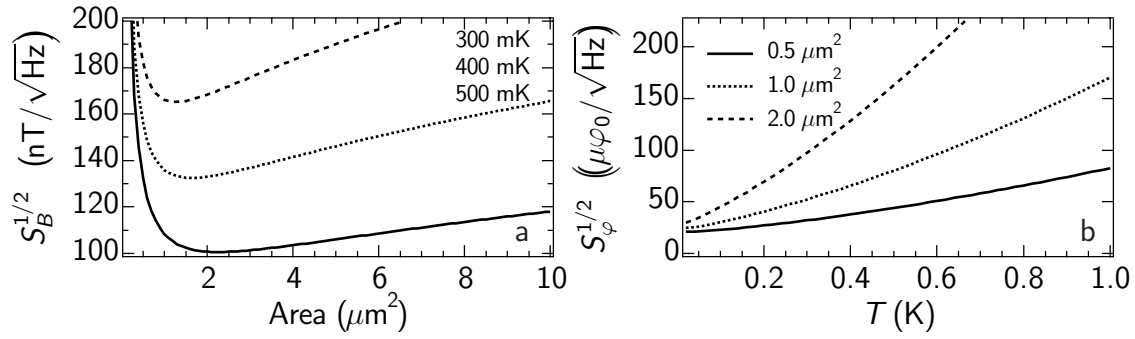
Figure 3.6: (a) Optimum magnetic field noise $S_B^{1/2}$ as a function of dot area. (b) Magnetic flux noise $S_\varphi^{1/2} = A S_B^{1/2}$.

of magnitude smaller.

Chapter 4

Pumping Electrons

The large majority of research into mesoscopic systems, including the first part of this dissertation, has focused on transport driven by an externally applied bias. The remainder of this dissertation focuses on the adiabatic quantum electron pump, exploring a class of transport in which the flow of electrons is driven by cyclic changes in the wave function of a mesoscopic system.

Before discussing the adiabatic quantum pump in chapter five, this chapter reviews other mechanisms that produce a dc response to an ac driving signal in coherent electron systems. The mechanisms reviewed here can be grouped into two categories: high frequency irradiation and low frequency gate modulation. Irradiating mesoscopic samples with microwave radiation drives the distribution of electron energies far from equilibrium which is often sufficient to cause dc transport. In open systems, the mesoscopic photovoltaic effect combines photon absorption and coherent random scattering to create a photocurrent which shows random sample specific fluctuations similar to UCF. In systems with tunnel barriers, inelastic photon assisted tunneling can create a dc current whose magnitude and direction are periodic in the shape distorting gate voltage. Low frequency current pumping in which the distribution of electron energies remains at (or very near) equilibrium is more subtile. A simple blanket irradiation will not cause net current flow in this regime. Instead, ac voltages are applied to the gates which define the system causing cyclic changes to its shape and/or its connection to the environment. Two ac voltages with a phase difference between them are required to create turnstile pumps in closed systems or adiabatic quantum pumps in open systems. As with the mesoscopic photovoltaic effect, current pumped by an adiabatic quantum pump has random sample specific fluctuations while turnstile pumps, like photon
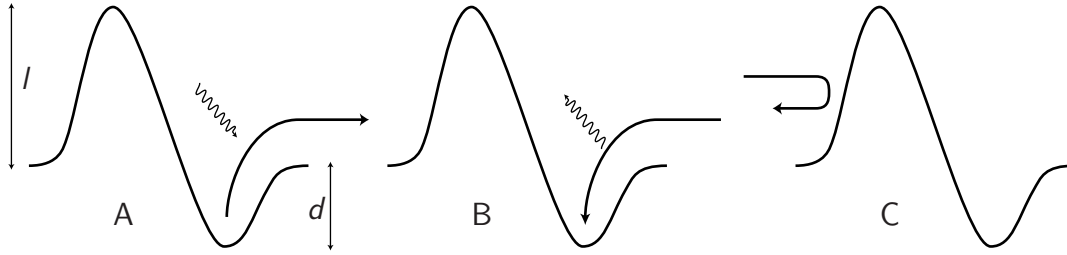
Figure 4.1: Asymmetric potential with height l and depth d as a model for the photovoltaic effect, demonstrating the three contributions to the photocurrent: photoexcitation (a) and electron trapping (b) which create a photocurrent toward the right, and reflection (c) which contributes a current in the opposite direction.

assisted tunneling, has a current whose magnitude and direction are determined by the control voltages.

4.1   The Mesoscopic Photovoltaic Effect

The classical photovoltaic (PV) effect has been well known in macroscopic crystals for over thirty years and is reviewed in [16]. When a non-equilibrium distribution of electron energies is created in a medium which lacks a center of symmetry, more electrons scatter in one direction than the other, creating a net current or, if measured in an insulated crystal, a photovoltage. Experiments in which laser illumination excites a non-equilibrium distribution in asymmetric crystals such as $LiNbO_3$ and $BaTiO_3$ produce photocurrents in the range of $0.1\,nA$ for each cm^2 of illuminated crystal.

The photocurrent is caused by asymmetric scattering of the excited electrons. We can model the potential as an asymmetric 1D well with barrier height $l \gg \hbar\omega$ and well depth $d < \hbar\omega$ (figure 4.1). There are three contributions to the current: photoexcitation of electrons from the well (a), trapping of electrons entering the well (b), and reflection of electrons from the well (c). To avoid creating a perpetual motion machine, these three contributions must cancel when the sample is in thermal equilibrium.

When a photon is absorbed, an electron exits the well, traveling to the right at velocity $v_0 = \sqrt{2(\hbar\omega - d)/m_e}$. Excited electrons travel toward the right until they scatter from another impurity a time τ later. Thus, if the excitation rate is pJ (where J is the light

intensity and p the probability of absorption), the photocurrent contributed will be

$$j_a = e v_0 p J \tau. \tag{4.1}$$

In order to maintain a steady state condition, as many electrons must become trapped in the well as are exited out of it. Because these electrons all come from the right (for $k_B T < \hbar \omega < l$), this contributes to the photocurrent in the same direction as photo excitation. Most of the electrons which become trapped will be in thermal equilibrium with the crystal, travelling at the thermal velocity v_T, and would have continued that way for time τ. Thus, electrons trapped will contribute a photocurrent of

$$j_b = e v_T p J \tau. \tag{4.2}$$

The final contribution to the photocurrent is the reflection of electrons that impinge on the potential from the left and is opposite in sign from the two previous terms. Since the flux of electrons arriving at the potential from the left is the same as that arriving from the right, $j_c = -2 j_b$ giving a final photocurrent

$$j_{\text{total}} = e p J (v_0 - v_T) \tau. \tag{4.3}$$

Note also that this photocurrent goes to 0 as it must when the sample is in thermal equilibrium with the radiation $v_0 = v_t$. Relaxing the assumption $h \gg \hbar \omega$ reduces the photocurrent by a factor η which characterizes the degree of asymmetry of the potential.

Fal'ko and Khmel'nitskiĭ predicted that the photovoltaic effect should be present in open mesoscopic samples without the need for an explicit asymmetry [34, 35] since the random scattering provided by impurities or a chaotic potential is inherently non-symmetric. Photocurrents due to this innate asymmetry generated in different regions of a macroscopic conductor add incoherently and average to zero. In a mesoscopic conductor with size $L \leq \ell_\phi$, the scattering is coherent and photovoltaic current can be measured. In the weak field limit ($e E L^2 g / \hbar \omega \ll 1$), the photocurrent can be estimated as

$$I_\phi \sim \eta e M / n^{1/2}. \tag{4.4}$$

where E is the applied ac electric field, M is the number of electrons excited per unit time and n is the number of contributions which add incoherently. In this limit an electron will

absorb only one photon so M is just the number of photons absorbed by the sample per unit time

$$M = \frac{E^2 L^2 g}{\hbar \omega}. \qquad (4.5)$$

The degree of asymmetry η is a function of the random scattering which is itself a sensitive function of external parameters such as energy and magnetic field. The photocurrent should thus display UCF-like fluctuations in both magnitude *and direction* in response to changes in these parameters. Like UCF, the scattering responsible for the photocurrent are correlated over an energy range $E_c = \hbar/\tau_D$ known as the Thouless energy [70] so that

$$n = \frac{\hbar \omega}{E_c} = \omega \tau_D \qquad (4.6)$$

independent energy ranges add incoherently. Finally, the typical values of η can be estimated as the ratio of the magnitude of the UCF to the sample conductance

$$\eta \approx \frac{e^2/h}{g} \qquad (4.7)$$

giving an estimate for the typical values of the photocurrent

$$I_\phi \approx \frac{e}{2\pi} \left(\frac{\omega}{\tau_D} \right)^{1/2} \left(\frac{EeL}{\hbar \omega} \right)^2. \qquad (4.8)$$

This estimate is replaced by an exact calculation in [35] and the photocurrent in the strong field limit is also explored along with the effects of temperature and decoherence. Because the direction of the photocurrent is random, $\langle I_\phi \rangle \approx 0$ and the typical value represents the standard deviation of the fluctuations around 0.

The photovoltaic effect has been measured in metal films [73] and Au rings [13] in a microwave cavity. The authors measured the open circuit photovoltage $V_\phi = I_\phi/g$ and find a that it behaves much as predicted by theory with aperiodic fluctuations as a function of B and of measurement temperature. The amplitude of the photovoltage was in good agreement with the theoretical prediction* although the temperature dependence was much weaker than predicted. Additional aspects of the photovoltage such as its dependence on

---

*$V_\phi \sim 4\,\text{nV}$ at $1.4\,\text{K}$ for a $1\,\mu\text{m}^2$ Ag sample in an $8.4\,\text{GHz}$ field at $20\,\text{V/m}$ compared to a theoretical prediction of $3\,\text{nV}$ [73].
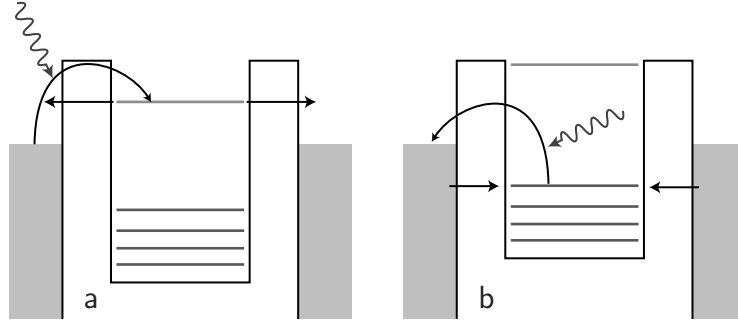
Figure 4.2: Photon assisted tunneling in the low frequency regime $\hbar\omega < \Delta$ allows transport which would be forbidden by Coulomb blockade in the absence of irradiation: (a) when the lowest unoccupied state is $\hbar\omega$ above the Fermi level of the leads and (b) when the highest occupied level is $\hbar\omega$ below the Fermi level of the leads. If the ac electric field couples symmetrically to the leads then the direction of current must be set with a small dc bias between source and drain. However, if the ac field couples more strongly to one lead, current can be created in the absence of dc bias.

E and the dephasing effect of microwaves are also reported. The authors do not, however, report any measurements of the frequency dependence of the photovoltage, presumably due to the difficulty of calibrating the microwave cavity for different frequencies.

4.2 Photon Assisted Tunneling

Microwave irradiation of quantum dots in the Coulomb blockade regime (see section 1.3.1) can lead to inelastic photon assisted transport (PAT). The peaks in conductance observed with no irradiation (figure 1.5) are split, developing sidebands in the presence of a microwave field. For photon energies below the energy level spacing of the dot[†], $\hbar\omega < \Delta$, PAT creates sidebands to the peaks in conductance where the ground state of the dot is $\hbar\omega$ above or below the Fermi level of the leads (figure 4.2). The photon assisted tunneling rate and thus the magnitude of these sidebands can be calculated [84] and the measured results agree qualitatively with the calculations [85]. Larger photon energies give PAT through excited states of the dot allowing a sort of PAT spectroscopy [85].

If the ac electric field couples asymmetrically to the source and drain reservoirs, a current is created in the absence of dc bias [61]. If PAT is only allowed to and from the left reservoir,

---

[†]$f \lesssim 2\,\mathrm{GHz}$ for a $1\,\mu\mathrm{m}^2$ GaAs/AlGaAs dot. The experiments in [61, 62, 85] were made in much smaller dots at $f \approx 20\text{–}60\,\mathrm{GHz}$ in both low and high frequency regimes.

the situation shown in figure 4.2a with the electron tunneling into the dot from the left and exiting through either side will cause a net current of half the tunneling rate to the left on one side of the conductance peak. On the other side of the peak, the situation shown in figure 4.2b with an electron tunneling out of the dot to the left and being replaced from either side creating a net current of the same magnitude to the right. Thus as the gate voltage is swept, the zero bias photocurrent will be small in the conductance valleys rising to a maximum in one direction when the lowest unoccupied state is $\hbar\omega$ above the Fermi level, returning to zero at the center of the peak itself (where the lowest unoccupied state is at the Fermi level) and rising to a maximum in the other direction when that state (now the highest occupied state) is $\hbar\omega$ below the Fermi level. Note that in contrast to the photovoltaic effect, the photocurrent is periodic in the gate voltage and does not show the same type of random aperiodic fluctuations seen in open systems.

4.3   Turnstile Pumping

The second class of devices which create dc transport from an ac excitation are the so called electron pumps. These devices work at low frequencies, typically in the MHz range, so that the ac excitation is slower than all of the characteristic times in the device. In this frequency range, the distribution of electron energies remains essentially in equilibrium and simply irradiating the device is not sufficient to drive a dc current. Instead, electron pumps require two (or more) control voltages, operating with a non-zero phase difference between them, to be applied to different regions of the device.

The most well characterized electron pumps are the turnstile pumps [63, 89] which, operating in the Coulomb blockade regime, transfer an integer number of electrons per cycle. Turnstile pumps have been realized in single quantum dots [63, 64] as well as chains of metal islands separated by tunnel junctions [88, 89]. The pumping cycle (figure 4.3) begins by isolating the device from one reservoir—for example by increasing the height of one tunnel barrier. The chemical potential of the device is lowered to bring an empty state in line with the Fermi energy in the reservoirs. That state is filled by tunneling from the side with the lower barrier, adding an electron. The device is then isolated from the reservoir which provided the electron, and the chemical potential is raised, forcing the electron into the opposite reservoir. The Coulomb blockade (section 1.3.1) assures that an integer number of electrons is pumped through the dot per cycle, yielding a net current of nef where n
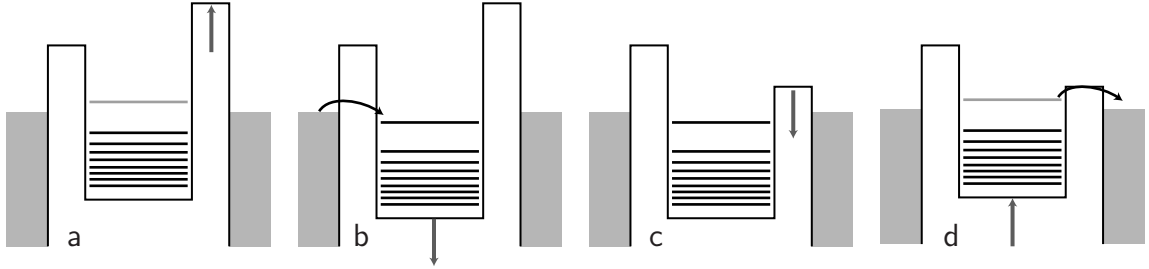
Figure 4.3: The pumping cycle of a turnstile pump. (a) The right tunnel barrier is raised preventing tunneling from the right reservoir. (b) The chemical potential is lowered until a state becomes available at the Fermi energy of the reservoirs. An electron tunnels in from the left reservoir. (c) The right tunnel barrier is lowered, allowing tunneling to the right reservoir. (d) The chemical potential is raised forcing an electron to tunnel to the right reservoir. Note that two control voltages operating out of phase (a $\pi/2$ phase difference is optimal) are required.

depends on the excursion of the chemical potential per cycle. The magnitude and direction of the pumping are determined by the control voltages; there are, in a first approximation, no fluctuations due to quantum mechanical effects. Note also that this pumping cycle requires two control voltages and is optimally effective with a phase difference of $\pi/2$ between them.

The control and quantization of current provided by turnstile pumps has stimulated their development for use in precision metrology [37]. Most of this work has been on multiple tunnel junction devices [89] with several metal islands separated by tunnel junctions. The large number of tunnel junctions helps to reduce the rare errors caused by the co-tunneling of electrons through more than one barrier at a time [59]. With these pumps, electrons can be transferred with an accuracy of 1 part in 10^8 [58] with photon assisted tunneling (section 4.2) thought to contribute much of the error [59]. The current produced is limited to $\sim 10\,\mathrm{pA}$ by the requirement that the control voltages change slowly compared to relaxation times in the dot. While this is too small for a practical current standard, a capacitance standard based on the turnstile pump has recently been proposed [58] with a relative capacitance error of 3×10^{-7}. Other pumping methods such as surface acoustic waves [103] are also being investigated with metrological applications in mind.

Chapter 5

The Adiabatic Quantum Electron Pump

The research into adiabatic electron pumping presented in this chapter was sparked by recent theoretical developments [18,98,113] extending to open systems a pumping mechanism first proposed by Thouless [6,105] for closed or otherwise gapped systems. Pumping occurs in a gapped system with a slowly changing potential

$$U(x,t) = U_1(t)f_1(x) + U_2(t)f_2(x) \tag{5.1}$$

with $f_1 \neq f_2$ where U_1 and U_2 are adiabatically slow periodic functions. The evolution of such a system can be described by its trajectory in the (U_1, U_2) plane and pumping is predicted to occur if the trajectory encloses non-zero area in this plane. The pumping is most easily seen in the example proposed by Thouless: a gapped 1D system with a traveling wave potential of wavelength a and period τ

$$U(x,t) = U_0 \sin\left(2\pi \left[\frac{x}{a} - \frac{vt}{\tau}\right]\right) \tag{5.2}$$

which can be decomposed into

$$U_{1,2} = U_0 \cos\left(2\pi \frac{vt}{\tau} + \phi_{1,2}\right) \tag{5.3}$$

$$f_{1,2} = \sin\left(2\pi \frac{x}{a} + \phi_{1,2}\right) \tag{5.4}$$

with $\phi_{1,2} = 0$, $\pi/2$. Because of the adiabaticity, as the potential moves along, the n electrons confined to each minimum move along with it, creating a current of nev/a with *no dissipation*. The Thouless potential traces a circle in the (U_1, U_2) plane but in general a system with a phase difference $\phi \neq 0$, π between U_1 and U_2 will enclose an area in the phase space and will pump. It should be emphasized that, like turnstile pumping (section 4.3), adiabatic pumping requires two control parameters with a non-zero phase difference between them. A single parameter can create only a standing wave which cannot transport charge.

The theory of Thouless has recently been extended [18, 113] to open systems where level broadening due to escape creates a continuum of states. Since there is no energy gap between full and empty states, the strict adiabatic condition cannot be met. Nevertheless, a deformation of the confining potential of a mesoscopic system that is slow compared with the relevant energy relaxation times can change the wave function of the system while maintaining an equilibrium distribution of electron energies and can in some sense be considered adiabatic. In systems connected to electron reservoirs by leads with one or more fully transmitting quantum modes, the wave function of system extends into the leads and the "adiabatic" changes can transport charge to or from the reservoirs. A periodic deformation that depends on a single parameter cannot result in net transport; any charge that flows during the first half-period will flow back during the second. On the other hand, a deformation of the form of equation 5.1 can break this symmetry and in general provide net transport. Because of the analogy with the Thouless pumping described above, it is hoped that at least part of this current flow will be dissipationless, perhaps allowing us to overcome the limits on bias driven current described in chapter three.

5.1   Measurements

Measurements of adiabatic pumping were made in three similar semiconductor quantum dots fabricated as described in section 1.2 and appendix A on heterostructures with 2DEGs at 56 nm (device 1) or 80 nm (devices 2 and 3) below the semiconductor surface (see appendix B for a detailed description of the heterostructure material and SEM images of these dots). All three dots had lithographic areas $a_{\text{dot}} \sim 0.5\,\mu\text{m}^2$ giving an average single particle level spacing $\Delta \sim 13\,\mu\text{V} \approx 150\,\text{mK}$. The three devices showed similar behavior and most of the data presented here are from device 3.
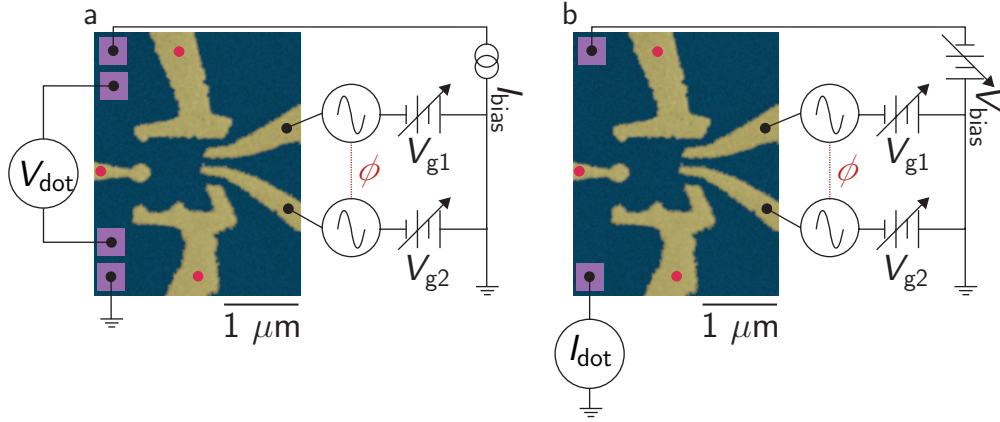
Figure 5.1: Schematic of the configurations for V_{dot} (a) and I_{dot} (b) measurements along with a micrograph of device 1. The bias (I_{bias}, V_{bias}) is set to zero for pumping measurements.

Figure 5.1 shows a micrograph of device one along with schematics of the measurement configurations. Voltages on the three gates marked with red dots control the conductances of the point contact leads. These were adjusted, following the procedure described in section 2.3, so that each lead transmitted $N \sim 2$ transverse modes, giving an average conductance through the dot of $\langle g \rangle \sim 2e^2/h$. The remaining two gates were used to create both the cyclic shape distortions necessary for pumping and dc shape distortions that allow ensemble averaging. Radio frequency function generators* with a computer controlled phase difference ϕ between them provided the cyclic deformations to which a computer controlled dc voltage V_g was added. To allow a sensitive lock-in measurement of the pumping signal, the signal from the frequency generators was chopped by a low frequency (93 Hz) square wave and either the voltage across the dot in an open circuit configuration V_{dot} (figure 5.1a) or the current through the dot I_{dot} (figure 5.1b) was measured synchronously. In either case an external bias (I_{bias} or V_{bias}) could be applied, allowing conductance to be measured without disturbing the measurement configuration. The external bias was set to zero for pumping measurements. Although I_{dot} is the more fundamental quantity, measurements of V_{dot} were made initially because it is experimentally more convenient. Comparisons of I_{dot} and V_{dot} measured under the same conditions confirm that $V_{\mathrm{dot}} \approx I_{\mathrm{dot}}/g$.

Except where noted, measurements were made at base temperature $T = 330\,\mathrm{mK}$, dot conductance $g \sim 2e^2/h \approx (13\,\mathrm{k\Omega})^{-1}$, ac frequency $f = 10\,\mathrm{MHz}$, and ac amplitude $A_{\mathrm{ac}} =$

---

*Hewlett-Packard model 3325 frequency generators with a frequency range $f = 0$–$20\,\mathrm{MHz}$
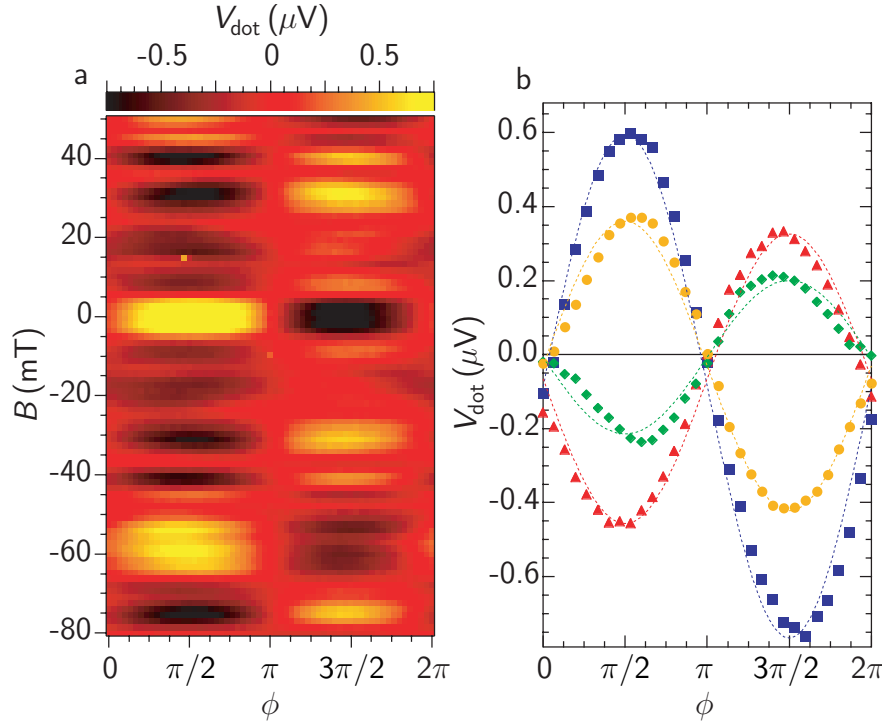
Figure 5.2: **(a)** Pumped dc voltage V_{dot} as a function of the phase difference ϕ between two shape-distorting ac voltages and magnetic field B. Note the sinusoidal dependence on ϕ and the symmetry about $B = 0$. **(b)** $V_{\text{dot}}(\phi)$ for several different magnetic fields (solid symbols) along with fits of the form $V_{\text{dot}} = A_0 \sin(\phi) + B_0$ (dashed curves).

80 mV peak to peak. For comparison, the gate voltage necessary to change the electron number in the dot by one is ~ 5 mV as determined by measurements of Coulomb blockade. Measurement were carried out over a range of magnetic fields $30\,\text{mT} \leq B \leq 80\,\text{mT}$ which allows several quanta of magnetic flux $\varphi_0 = h/e$ to penetrate the dot ($\varphi_0/a_{\text{dot}} \sim 10\,\text{mT}$) while keeping the classical cyclotron radius much larger than the dot size, $r_{\text{cyc}}[\mu\text{m}] \sim 80/B[\text{mT}]$.

The general characteristics of quantum pumping including antisymmetry about phase difference $\phi = \pi$, sinusoidal dependence on ϕ (for small amplitude pumping), and random fluctuations of pumping amplitude and direction as a function of perpendicular magnetic field are illustrated in figure 5.2. We quantify the amplitude of the pumping with the values A_0 and B_0 extracted from fits of the form $V_{\text{dot}}(\phi) = A_0 \sin\phi + B_0$ shown as dotted lines in figure 5.2b.
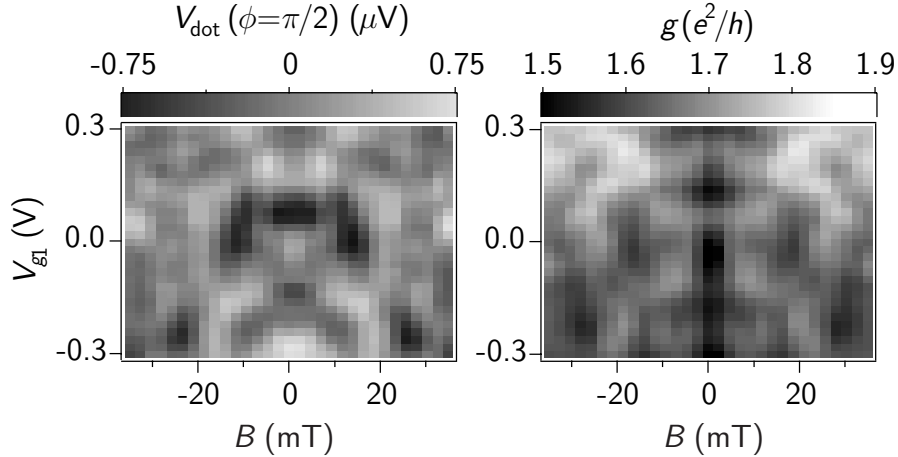
Figure 5.3: Plot of $V_{\text{dot}}(\phi = \pi/2)$ and g as a function of magnetic field and dc gate voltage. Note the symmetry of both fluctuations around $B = 0$ and their similar characteristic correlation scales. Note also that the fluctuations of pumping and conductance do not appear to be directly correlated.

The scale of the fluctuations of pumping amplitude and their symmetry about $B = 0$ are seen in the plot of $V_{\text{dot}}(\phi = \pi/2)$ as a function of B and V_{g1} (figure 5.3). The full symmetry of pumping which follows from time-reversal symmetry

$$V_{\text{dot}}(\phi, B) = -V_{\text{dot}}(-\phi, -B) \tag{5.5}$$

is analogous to the Landauer-Büttiker relations for conductance [113]. The symmetry observed in figure 5.3, $V_{\text{dot}}(\phi, B) = V_{\text{dot}}(\phi, -B)$, results from a combination of equation 5.5 and the sinusoidal dependence of V_{dot} on ϕ at low pumping amplitudes. The fluctuations of pumping amplitude, in response both to a changing magnetic field and to changes in the dc shape of the potential occur on a similar scale as the fluctuations of conductance. This scale is quantified as the half width at half maximum of the autocorrelation function $C(\Delta x) = \langle f(x)f(x + \Delta x)\rangle$. The HWHM of $C(\Delta B)$ in device 3 is 3.3 ± 0.4 mT for pumping and 3.9 ± 0.4 mT for the conductance fluctuations, comparable to and somewhat smaller than one flux quantum through the device, consistent with pervious experiments on conductance in similar dots [75]. Similarly, for both pumping and conductance, the HWHM of $C(\Delta V_g)$ is about 70 mV. Note also that the fluctuations of pumping and conductance do not appear to be directly correlated.
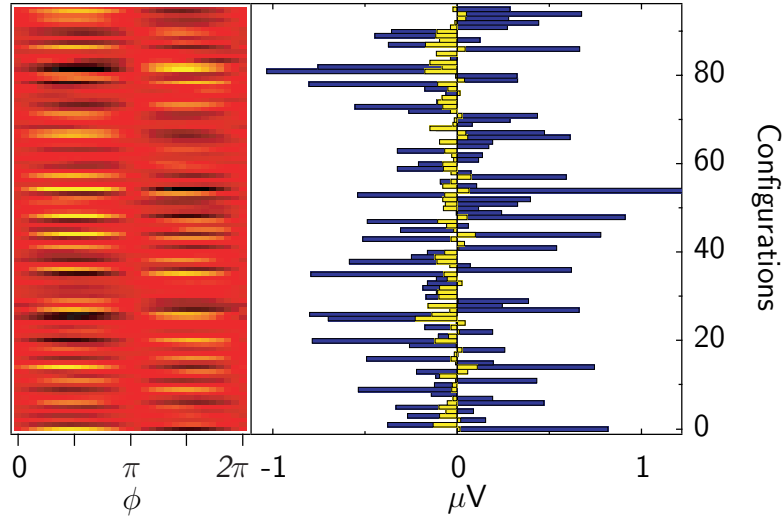
Figure 5.4: A typical data set corresponding to a single point in figures 5.5 and 5.6 along with fit parameters A_0 (blue) and B_0 (yellow) for each configuration.

Because the pumping amplitude fluctuates on both sides of 0 with equal likelihood for a given ϕ, $\langle A_0 \rangle$ is small and the typical pumping amplitude is instead characterized by the standard deviation of A_0, $\sigma(A_0)$. Each value of $\sigma(A_0)$ in figures 5.5 and 5.6 is based on fits to $V_{\mathrm{dot}}(\phi)$ for 96 independent configurations over B, V_{g1}, and V_{g2}. A typical data set for one of these points is shown in figure 5.4. For the data shown here, B_0 is a small correction but see also section 5.3 below. The data in figure 5.4 yield $\sigma(A_0) = 0.4\,\mu\mathrm{V}$ while $\langle A_0 \rangle = 0.01\,\mu\mathrm{V}$ and $\sigma(B_0) = 0.07\,\mu\mathrm{V}$.

The dependence of the pumping amplitude $\sigma(A_0)$ on pumping frequency is linear (figure 5.5a). This gives us confidence that our measurements are not corrupted by the influence of non-equilibrium pumping mechanisms such as the mesoscopic photovoltaic effect (see 4.1) which have a quadratic frequency dependence (to lowest order). For the above parameters, the linear dependence of adiabatic pumping has a slope of $40\,\mathrm{nV/MHz}$. Because $g \sim 2e^2/h$, this voltage compensates a pumped current of $3\,\mathrm{pA/MHz}$ or about 20 electrons per pump cycle.

Figure 5.5b shows the dependence of $\sigma(A_0)$ on the amplitude of the applied ac voltage A_{ac}. For weak pumping $\sigma(A_0)$ is proportional to A_{ac}^2. For stronger pumping, $\sigma(A_0)$ falls below A_{ac}^2 and appears consistent with $\sigma(A_0) \propto A_{\mathrm{ac}}^{1/2}$ for high A_{ac}. Note that the crossover occurs around $A_{\mathrm{ac}} = 80\,\mathrm{mV}$, near the characteristic voltage scale for fluctuations in the
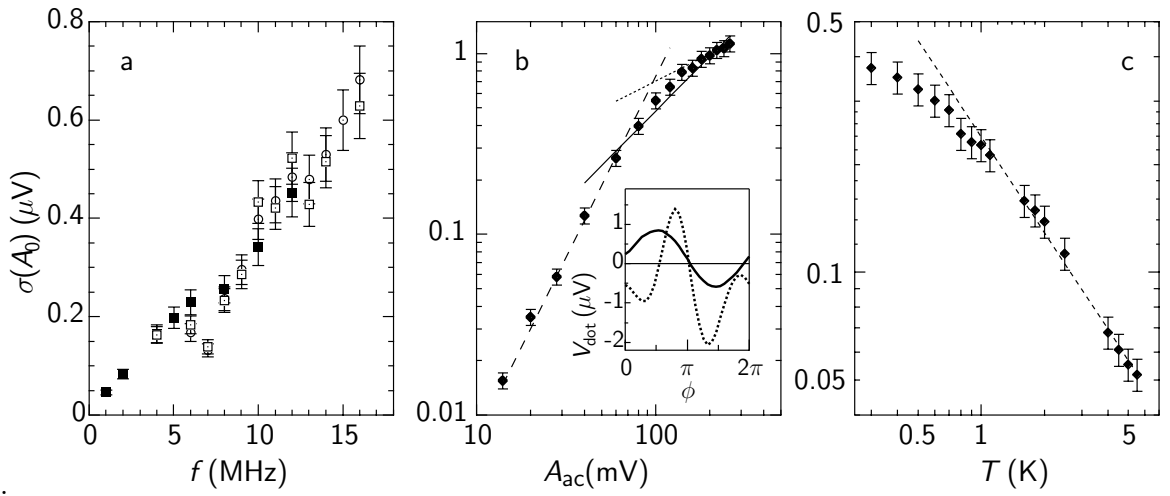
Figure 5.5: (a) Standard deviation of the pumping amplitude $\sigma(A_0)$ as a function of ac pumping frequency f. The dependence is linear with a slope of $\sim 40\,\mathrm{nV/MHz}$ for both devices 2 (solid symbols) and 3 (open symbols). (b) $\sigma(A_0)$ as a function of ac pumping amplitude along with fits to A_{ac}^2 below $80\,\mathrm{mV}$ (dashed line), and A_{ac} (solid line) and $A_{\mathrm{ac}}^{1/2}$ (dotted line) above $80\,\mathrm{mV}$. Inset: The sinusoidal dependence of $V_{\mathrm{dot}}(\phi)$ for small values of A_{ac} (solid curve $A_{\mathrm{ac}} = 100\,\mathrm{mV}$) becomes nonsinusoidal for strong pumping (dotted curve $A_{\mathrm{ac}} = 260\,\mathrm{mV}$ (c) $\sigma(A_0)$ as a function of temperature T with a power law fit. The rounding at low temperatures is consistent with an expected saturation below $\sim 100\,\mathrm{mK}$.
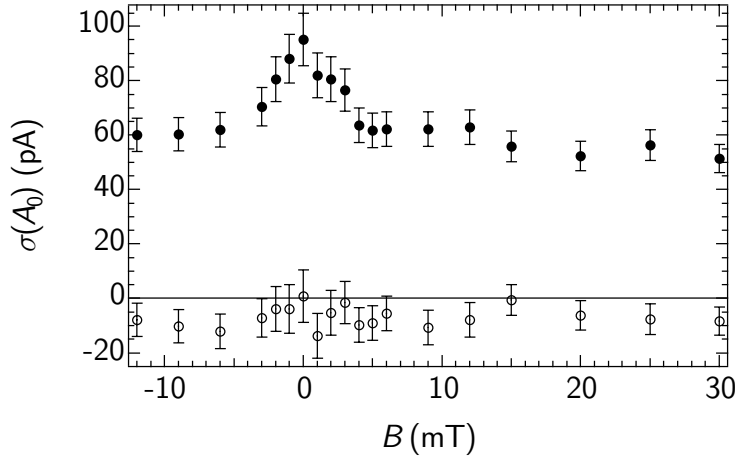
Figure 5.6: Average $\langle A_0 \rangle$ ($\circ$) and standard deviation $\sigma(A_0)$ ($\bullet$) of pumping strength. $\sigma(A_0)$ shows a peak around $B = 0$ almost twice its value away from zero field while $\langle A_0 \rangle$ remains close to zero.

pumping amplitude and the value of A_{ac} used to gather the other data presented here. At high A_{ac}, $V_{dot}(\phi)$ becomes non-sinusoidal as shown in the figure 5.5b inset. Notice that $V_{dot}(\phi = 0)$ remains close to zero for all pumping strengths whereas $V_{dot}(\phi = \pi)$ deviates from 0 at strong pumping.

The temperature dependence of $\sigma(A_0)$ is shown in figure 5.5c. At high temperatures (1–5.5 K), $\sigma(A_0)$ is well described by a power law,

$$\sigma(A_0) = 0.2T^{-0.9} \tag{5.6}$$

for $\sigma(A_0)$ in microvolts and T in kelvin. This behavior presumably reflects the combined influence of thermal smearing, which alone is expected to yield $\sigma(A_0) \propto T^{-1/2}$, and temperature dependent dephasing. A similar temperature dependence is found for the amplitude of conductance fluctuations in quantum dots [48, 49]. Below 1 K, the temperature dependence begins to round off, perhaps indicating a saturation at lower temperatures. A low-temperature saturation of pumping is expected when thermal smearing becomes less than lifetime broadening due to escape and dephasing $k_B T < \hbar(\tau_D^{-1} + \tau_\phi^{-1})$ [112]. For dots with two channels in each point contact, the results of section 2.3 and references [50] and [49] for dephasing times in similar dots yield an expected saturation at ~ 100 mK, consistent with the rounding seen in the data.

Finally, we investigate the effect of symmetry on the pumping. As discussed in sections 1.3.2 and 1.3.3, a central feature of mesoscopic physics is that the statistical properties of a fluctuating quantity depend on the symmetries of the system and little else. We measured pumped current as a function of magnetic field with a sampling finer than the characteristic scale of the fluctuations (figure 5.6). The average of A_0 is close to zero and has no outstanding features. On the other hand, $\sigma(A_0)$ shows a peak at $B = 0$ of almost twice its value away from zero field. The width of this peak, $\sim 3\,\mathrm{mT}$ HWHM, is comparable to the correlation field, suggesting that the peak is associated with the breaking of time reversal symmetry. Thus, as with conductance (equations 1.14 and 1.15), the pumping fluctuations are larger for the case of time reversal symmetry than for the case of broken time reversal symmetry.

5.2   Theory of the Adiabatic Quantum Pump

The work of Zhou and coworkers [113] and Brouwer [18] has recently extended the work of Thouless (see above and [105]) on adiabatic pumping to the regime of open systems, allowing at least qualitative comparison with the experiment. Following Brouwer's random matrix theory approach [18], we consider adiabatic changes to two parameters of the system X_1 and X_2. In the experiment above, these correspond to the two gate voltages which control the confining potential but they could just as well be the magnetic field, Fermi energy or any other parameter which changes the wavefunction of the system. Small variations of these parameters δX can transport charge into or out of the system through the leads. For a two lead system, a small adiabatic sinusoidal change $X_i = X_{i0} + \delta X_i e^{i\omega t}$ transports a charge through lead m

$$\delta Q = e \frac{dn_m}{dX_i} \delta X_i \tag{5.7}$$

with the emissivity into lead m

$$\frac{dn_m}{dX_i} = \frac{1}{2\pi} \sum_{q=1}^{2N} \sum_{p \in m} \mathrm{Im} \frac{\partial S_{pq}}{\partial X_i} S_{pq}^* \tag{5.8}$$

where $m = 1, 2$ labels the leads, p and q label the channels in the leads, and S is the scattering matrix for the system (see section 1.4.2) [23].
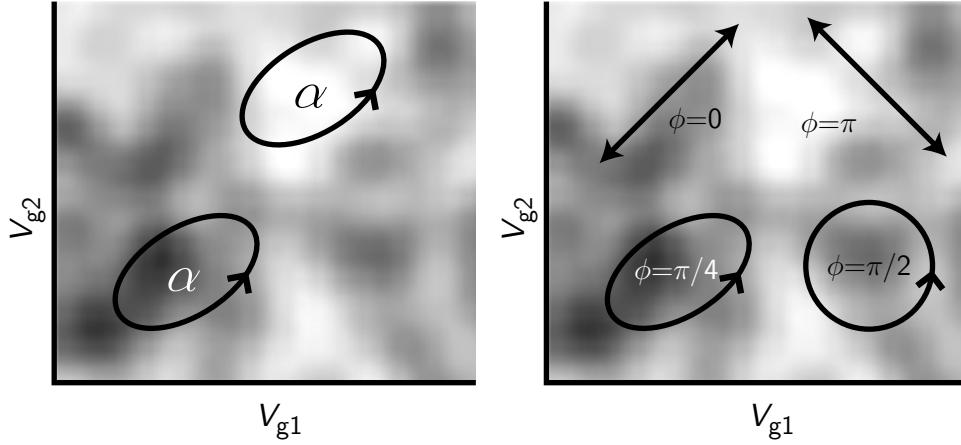
Figure 5.7: The pumped current is proportional to the area α of the trajectory of the system in (V_{g1}, V_{g2}) parameter space and the value of the integrand ξ in equation 5.10. Changing the dc value of V_{g1} or V_{g2} shifts the loop to a position with a different value of ξ, changing the pumped current (left). The area of the loop (and thus the pumped current) is proportional to $\sin \phi$ (right).

With two cyclically changing parameters, the total charge flowing through a lead in each period τ of the cycle is

$$Q(m) = e \int_0^\tau dt \left(\frac{dn_m}{dX_1} \frac{dX_1}{dt} + \frac{dn_m}{dX_2} \frac{dX_2}{dt} \right). \tag{5.9}$$

If we now consider the trajectory of the system in the (X_1, X_2) paramater space, this integral can be rewritten using Green's theorem in terms of the area in parameter space α enclosed by this trajectory

$$Q(m) = e \int_\alpha \xi \, dX_1 dX_2 \tag{5.10}$$

$$\xi = \frac{\partial}{\partial X_1} \frac{dn_m}{dX_1} - \frac{\partial}{\partial X_2} \frac{dn_m}{dX_2}. \tag{5.11}$$

Thus the current pumped is linked both to the parametric derivatives of the scattering matrix and to the area α enclosed by the system trajectory in the (X_1, X_2) plane. The former allows the machinery of RMT to be applied to the problem, including the calculation of the distribution of pumped current. The α dependence provides an intuitive picture for qualitative understanding of the experimental results. This integral can be visualized as a

the loop of area α traced out by the system superimposed on a background representing the values of ξ in the (V_{g1}, V_{g2}) parameter space. Changing V_{g1} or V_{g2} is equivalent to moving the center of the system trajectory over the background (figure 5.7a) and, since the scattering matrix changes with changes in the dot potential or magnetic field, the value of ξ inside the trajectory will fluctuate, giving rise to the fluctuations in pumping amplitude. Since changes in S are also at the root of UCF, it is not surprising that pumping and conductance fluctuations have the same typical scales. However, since g depends on the square of the elements of S (equation 1.10) while the pumped current depends on its derivatives through the emissivity (equation 5.8), it is not clear that their fluctuations should be correlated. Detailed theoretical analysis predicts is that they should be correlated at $B = 0$ but not away from zero magnetic field [18,21]. Note also that $Q(m)$ is the charge pumped *per cycle*, implying a linear frequency dependence for the pumping, in agreement with the experiment (figure 5.5a).

For a small pumping amplitude, A_{ac} less than the correlation length of the pumping fluctuations, ξ will be essentially constant within the loop and the pumped current simply proportional to α. Since $\alpha \propto \sin(\phi)$, this explains the sinusoidal dependence of the pumped current on ϕ. The proportionality of the pumped current to α at low amplitudes also explains the A_{ac}^2 dependence seen in figure 5.5b since A_{ac} is the diameter of the loop. As the size of the loop approaches the scale of the fluctuations in ξ, the pumped current departs from this A_{ac}^2 dependence. For strong pumping, the loop will enclose many fluctuations of ξ. If these fluctuations are uncorrelated, one expects the pumped current to be proportional to the square root of the number of fluctuations enclosed, $\sigma(A_0) \propto \sqrt{\alpha} \propto A_{\text{ac}}$. Instead we find a dependence which is slower than linear and appears to be consistent with $\sigma(A_0) \propto A_{\text{ac}}^{1/2}$. This unexpectedly slow dependence may result if significant heating and dephasing of electrons occurs as a result of the strong pumping. It has been suggested by Avron [9] and others that the fluctuations of ξ at non-zero magnetic field are not uncorrelated but rather pair up in such a way that the average ξ in any large area tends toward zero. In that case, only small fluctuations of ξ around the perimeter of the loop will contribute to the pumping current which would then scale as the length of the loop perimeter or $A_{\text{ac}}^{1/2}$. Clearly, further research both theoretical and experimental is required to resolve this difference between experiment and the naïve theory.
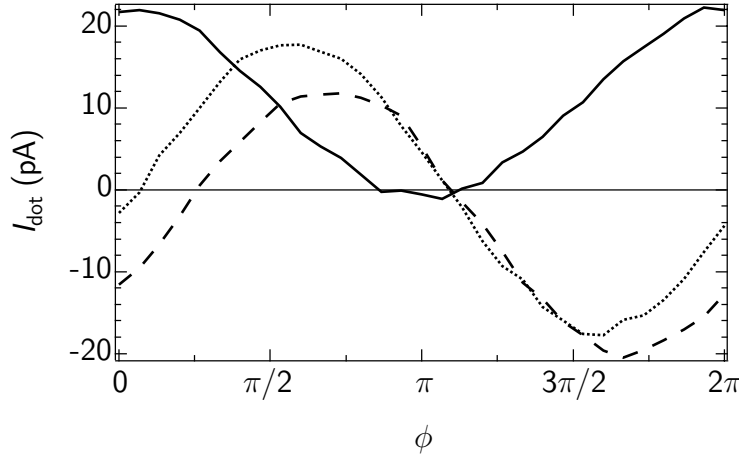
Figure 5.8: Non-sinusoidal $I_{\text{dot}}(\phi)$ for several different magnetic fields. Both the shape and the offset vary with B and V_g but I_{dot} is often near zero at $\phi = \pi$.

5.3   Rectification

Unfortunately, adiabatic pumping is a difficult phenomenon to measure and this experiment faced many technical challenges. The biggest problem was the existence of current with zero phase difference between the ac signals. Although in the data shown in section 5.1, some current is pumped even at $\phi = 0$ (equivalent to a single pin), $I_{\text{dot}}(\phi)$ remains essentially sinusoidal and the offset is a small correction. In some devices tested, however, the current pumped at $\phi = 0$ is not small and $I_{\text{dot}}(\phi)$ is distinctly non-sinusoidal often resembling $I_{\text{dot}}(\phi) \propto 1 - \cos(\phi)$ or some combination of sin and $1 - \cos$ terms (figure 5.8), often with I_{dot} near zero at $\phi = \pi$. The shape of the curve and the amount of current at $\phi = 0$ fluctuate with small changes in magnetic field or other parameters.

Zero phase difference is equivalent to a single pumping gate and in devices which showed this non-sinusoidal behavior, current was created when ac voltage was applied to a single gate. This current appears to be due to inadvertent capacitive coupling of the ac voltage to the electron reservoirs, creating an ac bias

$$V_{\text{bias}} = V_0 \sin(\omega t) \tag{5.12}$$

where ω is the MHz range angular frequency of the applied ac voltage. Figure 5.9 shows a model electrical schematic of the combination of stray capacitance with resistance from
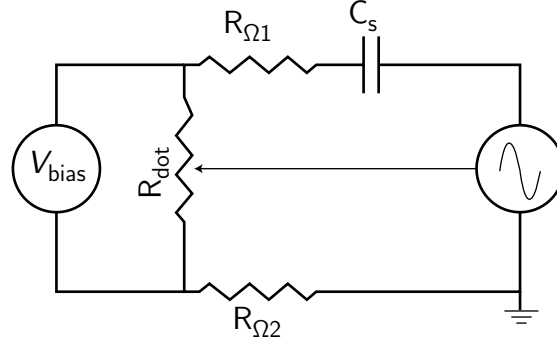
Figure 5.9: Electrical schematic for rectification model of current generated with a single ac pumping gate. The combination of stray capacitance between the gate and the electron reservoir C_s and the resistances of the dot R_{dot} and the ohmic contacts R_Ω form a high pass filter coupling the ac voltage applied to the gate into an ac bias voltage V_{bias} on the dot. Since the resistance of the dot is also changed by the applied ac voltage, the ac V_{bias} is rectified, producing a dc current

the dot and the ohmic contacts acting as a high pass filter for the ac signal. The ac gate voltage also changes the shape of the dot potential, creating conductance fluctuations at the ac frequency; the instantaneous conductance is a function of dc gate voltage V_g as well as the ac excitation

$$g = g\left[V_g + A_{ac}^* \sin(\omega t)\right] \tag{5.13}$$

where A_{ac}^* is the amplitude of the ac voltage felt on the gate itself (as opposed to A_{ac} which is the nominal ac voltage set at the voltage source) and V_g is the dc voltage on that gate. Since the changes in g and the inadvertent bias occur at the same frequency and are in phase[†], the current produced in the rectification does not average to zero:

$$I_r = \int_0^{2\pi} V_0 \sin(\omega t)\, g\left[V_g + A_{ac}^* \sin(\omega t)\right]\, d(\omega t). \tag{5.14}$$

For $A_{ac}^* \ll V_g$, this reduces to

$$I_r \approx V_0\left[g(V_g + A_{ac}^*) - g(V_g - A_{ac}^*)\right] \approx \frac{dg}{dV_g}. \tag{5.15}$$

[†]or at least have a fixed phase relationship. A phase shift may be imposed by the capacitive coupling to the reservoirs.
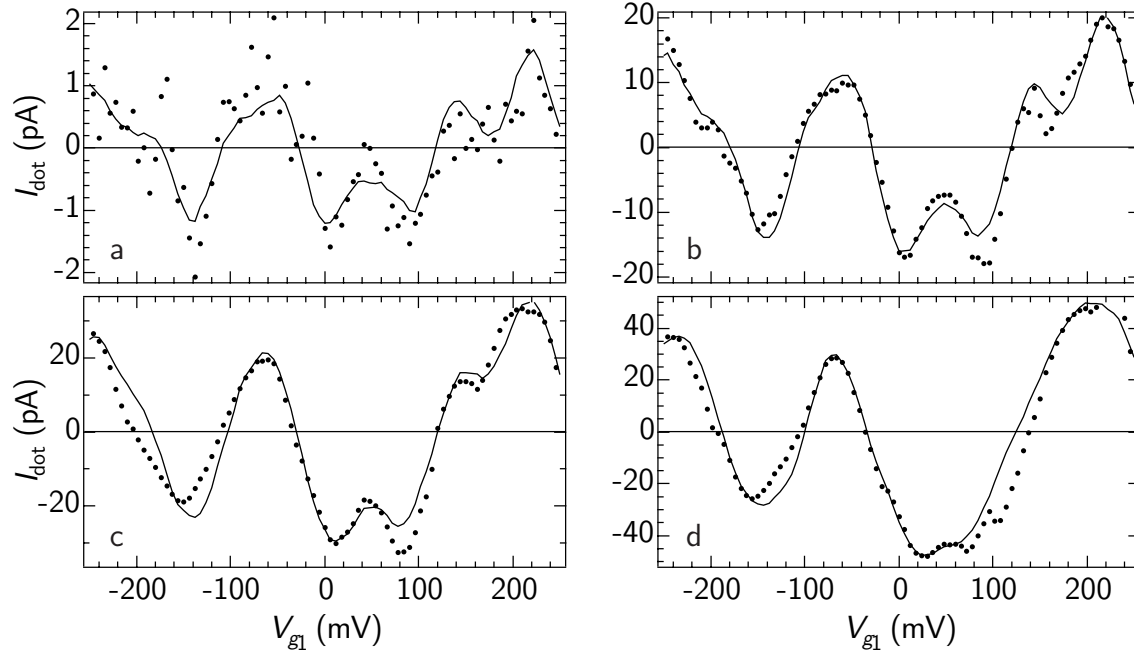
Figure 5.10: Comparison between measured I_{dot} with a single ac excitation and rectification current I_r. Data points represent I_{dot} measured with $A_{ac} = 20$ (a), 80 (b), 120 (c), and 160 mV (d); solid lines are a fit to of equation 5.14 to the data with two free parameters, A_{ac}^* and V_0 and using measured values of $g(V)$.

Figure 5.10 shows a comparison between the I_r calculated from equation 5.14 and the measured current through a dot with a single ac excitation. With the ac voltage turned off, conductance is measured as a function of V_g over a range larger than that shown in the figure. The ac voltage is then turned on and $I_{dot}(V_g)$ is measured at zero applied bias for various values of A_{ac}. Each trace is fit to the form of equation 5.14 with two free parameters, A_{ac}^* and V_0. Both of these parameters increase roughly linearly with A_{ac}, $A_{ac}^* \approx 1/2 A_{ac}$ and $V_0 \approx 10^{-5} A_{ac}$ (figure 5.11). This produces a rectification current on the order of 10 pA, similar to the the pumping current measured in other devices.

We tried several techniques in an effort to reduce the rectification current. We first focused on reducing the ac electric field on the reservoirs by altering the design of the dots. Dots were fabricated with large grounded metal regions between the gates carrying the ac voltages and all other gates in an attempt to create a waveguide for the ac signal. The presence of these metal regions and their grounding configuration seemed to have
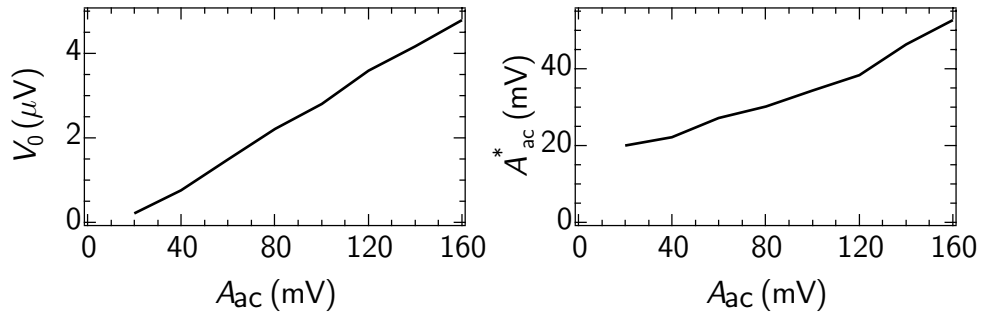
Figure 5.11: Parameters A_{ac}^* and V_0 extracted from the fits to data shown in figure 5.10.

little impact on the rectification, perhaps because the ac electric field was coupling in from the unshielded bond wires ($\sim$ 0.5–1 mm bare Au wire passing within 1 mm of the ohmic contacts).

Attempts to reduce rectification by reducing the resistance of the ohmic contacts were somewhat more successful. Well below the resonant frequency of the high pass filter (figure 5.9), V_0 should be proportional to the resistance of dot and ohmic contacts. In addition, all of the devices in which the rectification did not interfere with the adiabatic pumping had ohmic contacts with resistance below $\sim$200 Ω while devices with significant rectification had much higher ohmic resistances of 500–1000 Ω. A series of devices was fabricated with extremely low ohmic resistances, 10–50 Ω, and several of these showed low rectification currents. Unfortunately, the 2DEG on which these devices was manufactured was electrically noisy, rendering most of these devices unusable. I hope that the development of low resistance ohmic contacts on a quiet 2DEG will allow the measurement of adiabatic pumping without interference from rectification.

Chapter 6

Discussion and Conclusions

6.1   Summary of Research

The research completed for this dissertation focused on two major areas. In the first area, the study of electron phase coherence in open quantum dots, weak localization was applied for the first time to the determination of the phase decoherence time in quantum dots. While weak localization is the standard tool for determining decoherence time in 1D and 2D diffusive systems, theoretical developments [12, 20] have only recently made its application possible in quantum dots. The dephasing time in open quantum dots was found to have a $\tau_\phi \propto AT^{-1} + BT^{-2}$ temperature dependence, clearly slower than the T^{-2} dependence observed in ballistic 2D systems and predicted for closed dots. In the absence of any theoretical predictions for open quantum dots, this temperature dependence suggests the presence of a Nyquist-like dephasing mechanism in these systems.

With an eye toward technological applications of quantum dots, we measured the effect of increased bias on the phase coherence time and other properties of a quantum dot. The effects of increased bias are well described by an effective temperature which can be derived from a balance of Joule heating and cooling by out diffusion of hot electrons from the dot. Further, there are good reasons to believe that this effective temperature actually represents the electron temperature inside the device. Using this effective temperature model, along with the known properties of quantum dots, we analyze a quantum dot magnetometer as an example of optimizing a device for a specific practical function. While the quantum dot magnetometer will not supplant SQUIDs in the near future, it could be competitive with other normal state techniques for magnetometry.

The second part of the research focuses on a completely different form of transport, adiabatic electron pumping which has the potential of overcoming some of the heating imposed limits of bias driven transport. Measurements of a current (or voltage) resulting from cyclic changes in the shape of the dot potential (at MHz frequencies) in the absence of an imposed bias are presented. The characteristics of this pumping firmly identify it with theoretical predictions for adiabatic pumping, although the behavior at high pumping amplitudes still requires explanation.

Finally, some of the problems with measuring adiabatic pumping are presented. In particular, a current generated in some devices by rectification of the pumping control voltages complicates the observation of adiabatic pumping. Some progress has been made in designing devices which avoid this problem, but much more needs to be done.

6.2   Future Directions

Although not observed in the experiments presented here, a widely observed saturation in the decoherence time at low temperatures (including subsequent observations in our lab) [17, 28, 49, 81] remains one of the most active and controversial areas in mesoscopic physics today [5, 60, 80] and clearly requires further study.

In the area of adiabatic pumping much remains to be done. The first, essential experimental step is to design devices which will reliably exhibit adiabatic pumping without interference from other effects. Some progress has been made with low resistance ohmic contacts but this goal remained elusive throughout my research. Once this problem is solved, a great many experiments remain. One of the first is to understand the disagreement between the data and the naïve theory of pumping at high pumping amplitudes. Several explanations have been proposed, some with striking experimental consequences which need to be tested. In addition, theoretical predictions about correlations between conductance and pumping fluctuations as well as the distributions of pumping current [18] remain to be tested.

Beyond this, experiments to establish the role of decoherence and dissipation in adiabatic pumping are required. If pumping is to be used to circumvent the limitations of bias driven current, the limits on pumped current must also be established.

Appendix A

Device Fabrication

The entire quantum dot fabrication procedure beginning with the receipt of a wafer of MBE grown heterostructure is carried out by students in the Marcus Lab in a small clean room in the Ginzton Laboratories at Stanford. In addition to myself, Sara Cronenwett, Joshua Folk, Andy Huibers, Sebastian Maurer, Sam Patel, and Duncan Stewart contributed both to process development and to the actual processing of samples measured for this dissertation. Quantum dot fabrication consists of the following steps:

1. cleave a small *chip* from the wafer

2. etch *mesas* to isolate neighboring devices (optical lithography)

3. deposit and anneal *ohmic contacts* (optical lithography)

4. deposit the gates which define the dot (electron beam lithography)

5. connect the gates to bond pads (optical lithography)

6. glue chip into chip carrier

7. bond devices of interest

Each of these steps will be discussed in detail below. Figure A.1 shows micrographs of a typical device at four stages of magnification and figure A.2 shows two bonded chips side by side in a chip carrier.
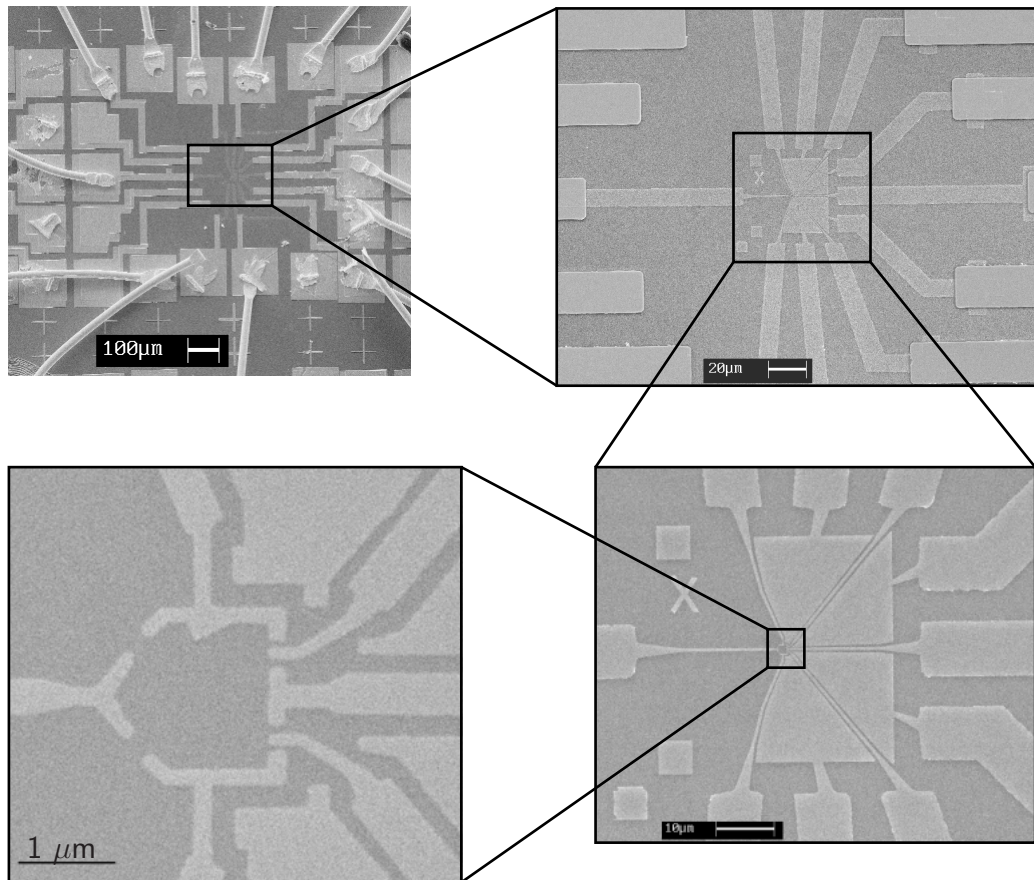
Figure A.1: Electron micrographs of a typical device at increasing magnification.
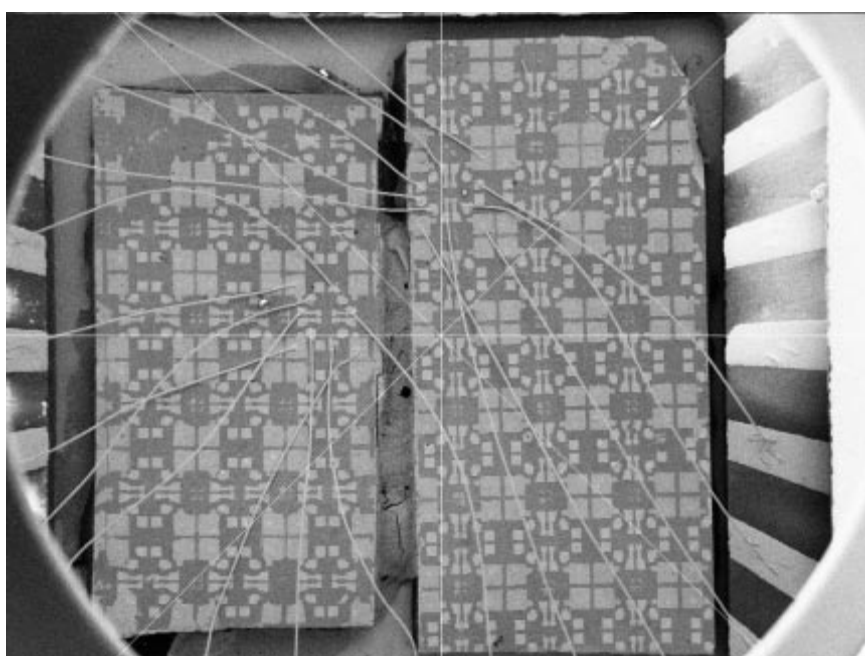
Figure A.2: Electron micrograph of of two chips side by side in a chip carrier. The circular rim is the final aperture of the electron microscope.

A.1   Electron Beam Lithography

Electron beam lithography and metal liftoff are used to create the gates which define the dot itself as well as the interconnects between these gates and the larger scale features created with optical lithography. A plastic resist (in our case, polymethyl methacrylate PMMA) is exposed to a controlled dose of 25 keV electrons in the desired pattern. The pattern is then developed with a solvent in which only the exposed resist is soluble, leaving a coating of resist with holes in the shape of the desired pattern. Metal is then evaporated, coating the whole surface of the sample. Finally, the remaining resist is dissolved taking its coating of metal with it, leaving metal in the desired pattern. Many variations on the basic process were tried over the course of this work, but the procedure detailed here using a single layer of PMMA with a molecular weight of 950k is by far the most reliable even though the lack of undercut causes some tearing at liftoff.

A converted Leica Leo Stereoscan 440 electron microscope along with the Nabity Nanometer Pattern Generation System (NPGS) and home built software generate and control the electron beam. Because this is an electron microscope some lack of flexibility is to be expected compared with a purpose built electron beam writing machine. The major problems are the limitation of stage repeatability to $\pm 5\,\mu$m which must be taken into account in device design and the inability to automatically align multiple fabrication steps. In addition, because of the multiple layers of software required, the writing process is fairly tedious with a large margin for human error. For these reasons, many members of the Marcus group now prefer the Hitachi electron beam writer located in the Center for Integrated Systems at Stanford.

The pattern to be written is designed in Design CAD and transferred to the NPGS computer. From there, a *run file* is created for each pattern to be written, defining the parameters of the exposure such as the magnification, desired electron dose, measured beam current, etc. In general, we write the smallest features of the dot at $4400 \times$ magnification and $\sim$100 pA beam current which gives a minimum feature size of $\sim$100 nm for lines and $\sim$50 nm for gaps. Larger features are written at $370 \times$ magnification and a 10 nA beam current. Normal exposure doses are around $300\,\mu$C/cm^2 but this varies and a matrix of exposure levels is typically run before each fabrication run to determine the best exposure level. A typical pattern file along with a micrograph of the dot produced are shown in figure A.3.
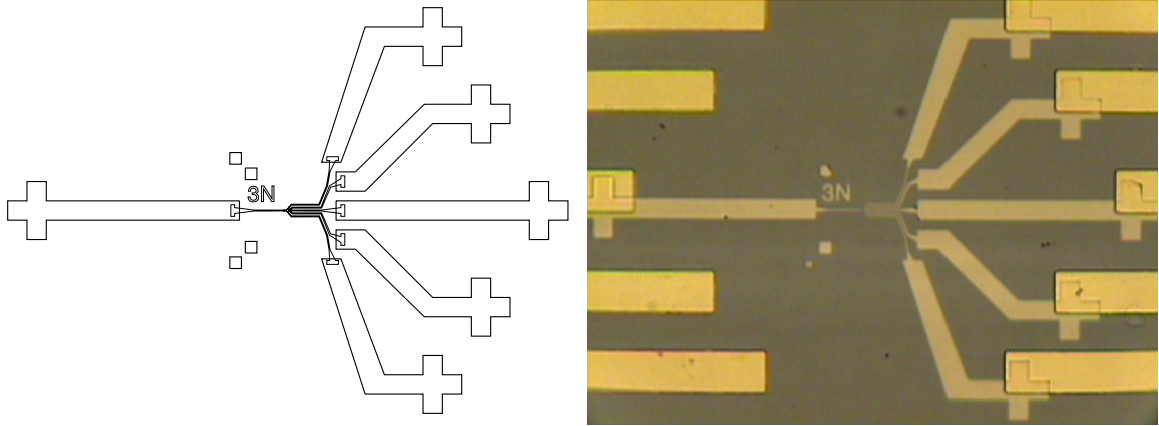
Figure A.3: Electron beam fabrication pattern as designed (left) and the corresponding fabricated dot (right). The lettering is $8\,\mu$m high.

The sample is prepared by cleaning with a three solvent clean (5 minutes each in ultrasound in boroethane, acetone, and methanol) and drying for 5 minutes at $120\,^{\circ}$C. A 4% solution of 950k molecular weight PMMA in chlorobenzene is spun so that a layer of PMMA about 120 nm thick remains on the sample. The spin speed required varies as the concentration of PMMA changes over time; a good starting point (April 1998) is 6500 rpm for 30 s but this should be tested on practice samples every time. The sample is then baked for 30 minutes or more at $180\,^{\circ}$C to drive off the remaining solvent.

After the sample is loaded into the Leica and the SEM is pumped down, a focal plane is established by measuring the focus at three corners of the sample. Home built software then calculates the position and focal length for each pattern to be written. In general, arrays of 20–100 dots are written on each chip. A DOS batch file is then created which calls NPGS to write each pattern and home built software to control the stage between patterns.

When the writing is complete, the PMMA is developed in a solution of 3:1 isopropanol:methyl isobutyl ketone with 1.3% methyl ethyl ketone added. The chip is then loaded into a thermal evaporator where 25 Å of Cr followed by 120 Å of Au are evaporated. When the sample has cooled, it is placed in an acetone bath to complete liftoff. Because there is no undercut, liftoff generally proceeds with some tearing of the metal at the edges of the pattern. Often, the application of ultrasound ($\sim$10 s at a time) is required to complete liftoff.
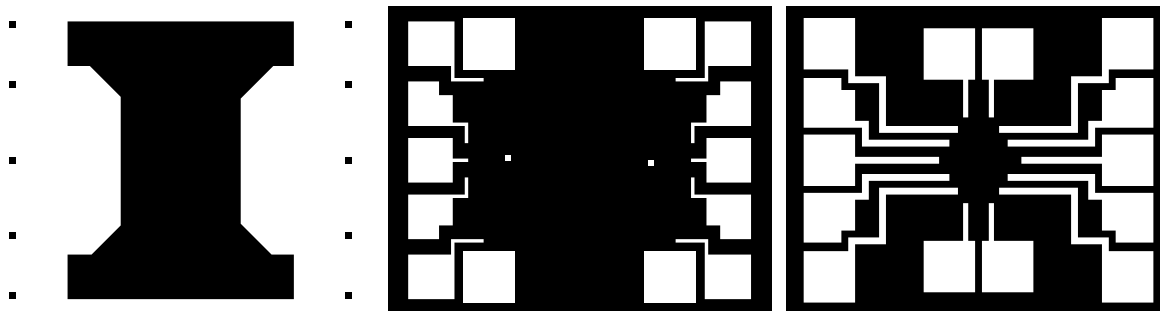
Figure A.4: The three layers of an optical lithography mask for quantum dot fabrication: mesa (left), ohmic contacts (middle), and bond pad interconnects (right). Dark areas represent areas of Cr on the mask which are opaque to ultraviolet light. Note that only the four square holes in the ohmic layer are fall on the mesa where they can make contact to the 2DEG. The rest facilitate wire bonding by increasing the adhesion of the bond pads which overly them.

A.2   Optical Lithography

The general outline of the optical lithography process is similar to the electron beam lithography described above. A photosensitive plastic is exposed to light in the desired pattern and developed to create a mask for either metal liftoff or for etching of the GaAs. Our process has been optimized to be reliable, with a large undercut to facilitate liftoff. The fairly low resolution limit of this process, $\sim 3\,\mu$m, is not a problem for us since all smaller features are fabricated using the electron beam.

After cleaning the sample with a three solvent clean (using ultrasound unless it would damage features already deposited on the chip) and drying at $120\,^{\circ}$C for 5 minutes, the photoresist (Shipley 1813) is spun on to the chip at $7000\,$rpm for $30\,$s, yielding a thickness of about $1\,\mu$m and the sample soft baked at $90\,^{\circ}$C for 10–20 minutes to drive off the remaining solvent. It is very important not to hard bake the photoresist at a higher temperature since the resist becomes insoluble in acetone. If liftoff is desired, the sample is then soaked in chlorobenzene for 15 minutes which makes the top layer less soluble in the developer, leading to a generous undercut. After another 5 minute bake at $90\,^{\circ}$C, the sample is ready to be exposed.

The sample is exposed to ultraviolet light for $25\,$s using a Karl Süss MB-3 mask aligner. This overexposes the resist giving high reliability and patterning to the edges without the need for a separate edge bead removal stage, at the price of reduced resolution. The mask

itself is a glass plate coated with Cr in the areas where no metal (or no etching) is desired. The three layers of a typical mask: mesa, ohmic contacts, and bond pad interconnects are shown in figure A.4. After exposure, the resist is developed in Microposit concentrated developer diluted 1:1 with water for 1 minute 15 s.

If metal is to be deposited, the surface is then cleaned using a short oxygen plasma etch (0.08 min at 50% power) and a 1 minute soak in 20:1 buffered oxide etch (a buffered HF solution). The sample is then loaded into the thermal evaporator and metal is deposited. For the bond pad interconnects, 200 Å of Cr are deposited followed by 2500 Å of Au. Ohmic contacts require 50 Å Ni, 1200 Å AuGe eutectic, 250 Å Ni, and 1500 Å Au. After liftoff in acetone, which generally proceeds quickly and without the need for ultrasound, interconnects are complete. Ohmic contacts must be annealed to make contact to the 2DEG. The optimum annealing temperature and time vary from heterostructure to heterostructure and must be established for each new wafer used. An average anneal heats the chip to 410 °C for 20–50 s and produces a contact with a resistance of 10–1000 Ω.

Etching of the mesas is done in a dilute solution of sulfuric acid, 1:8:240 mixture of $H_2SO_4 : H_2O_2 : H_2O$. The etch rate depends fairly sensitively on both the strength of the solution and the temperature and must be calibrated each time. Typically, the etch removes all of the AlGaAs layer to the depth of the 2DEG however, a much shallower etch is sufficient to isolate the devices.

A.3   Packaging and Wire Bonding

Finished chips are glued with PMMA into 28 pin non-magnetic ceramic chip carriers which can be inserted into corresponding sockets installed in all the cryostats in the lab. An ultrasonic wedge bonder with 25 μm Au wire is used to connect the bond pads on the device to the chip carrier (figure A.2). Note that ohmic metal is placed under the bond pads to facilitate bonding. Since the pads are off the mesa, this ohmic metal does not make contact to the 2DEG lending its superior adhesion to the bonding process while not interfering with the operation of the device.

Appendix B

Quantum Dot Inventory

B.1 Heterostructures

The heterostructures used in this research were grown by Ken Campman and Kevin Maranowski in the group of Arthur Gossard at UCSB. Many heterostructures were tried but only a few provided useful data. The most frequent problem is with telegraph noise, probably due to thermally activated rearrangement of charge in the doping layer. In addition, difficulty making ohmic contact, non-uniform 2DEG density, and insufficient mobility can preclude the use of a particular heterostructure. The growth profiles and measured electron mobility and density for the four heterostructures which provided data for this dissertation are given below.

B.1.1 Wafer 931217B

This heterostructure was particularly useful for measurements of adiabatic pumping, perhaps due to the low resistance of its ohmic contacts.

2DEG depth	$80\,\mathrm{nm}$
sheet density	$n = 2.6 \times 10^{11}\,\mathrm{cm}^{-2}$
mobility	$\mu = 0.26 \times 10^6\,\mathrm{cm}^2/\mathrm{V\,s}$
ohmic contacts	$R \approx 175\text{--}500\,\Omega$

50 Å	GaAs Cap
500 Å	$Al_{0.3}Ga_{0.7}As$
	δ dopant layer, Si, $n = 5 \times 10^{12}\,cm^{-2}$
250 Å	$Al_{0.3}Ga_{0.7}As$ spacer
8000 Å	GaAs
800 Å	Superlattice: 20 periods of 20 Å GaAs/20 Å $Al_{0.3}Ga_{0.7}As$
1000 Å	GaAs
	Substrate: semi-insulating GaAs

B.1.2   Wafer 940708A

This heterostructure was used for the measurements of decoherence. Perhaps due to its depth below the surface, it formed very clean point contacts and quantum dots with little switching noise.

depth	160 nm
sheet density	$n = 1.8 \times 10^{11}\,cm^{-2}$
mobility	$\mu = 0.9 \times 10^{6}\,cm^2/V\,s$

100 Å	GaAs Cap
1000 Å	$Al_{0.3}Ga_{0.7}As$
	δ dopant layer, Si, $n = 2.5 \times 10^{12}\,cm^{-2}$
500 Å	$Al_{0.3}Ga_{0.7}As$ spacer
8000 Å	GaAs
3000 Å	Superlattice $GaAs/Al_{0.3}Ga_{0.7}As$
3000 Å	GaAs
	Substrate: semi-insulating GaAs

B.1.3 Wafer 960924C

This heterostructure was used for adiabatic pumping measurements. Note the low resistance of its ohmic contacts

depth	$57\,\mathrm{nm}$
sheet density	$n = 7.3 \times 10^{11}\,\mathrm{cm}^{-2}$
mobility	$\mu = 0.37 \times 10^6\,\mathrm{cm}^2/\mathrm{V\,s}$
ohmic contacts	$R \approx 100\text{–}200\,\Omega$

$50\,\text{Å}$	GaAs Cap
$300\,\text{Å}$	$\mathrm{Al_{0.3}Ga_{0.7}As}$
	δ dopant layer, Si, $n = 8 \times 10^{12}\,\mathrm{cm}^{-2}$
$220\,\text{Å}$	$\mathrm{Al_{0.3}Ga_{0.7}As}$ spacer
$10000\,\text{Å}$	GaAs
$800\,\text{Å}$	Superlattice: 20 periods of $20\,\text{Å}$ GaAs/$20\,\text{Å}$ $\mathrm{Al_{0.3}Ga_{0.7}As}$
$500\,\text{Å}$	$\mathrm{Al_{0.3}Ga_{0.7}As}$
$1000\,\text{Å}$	GaAs
	Substrate: semi-insulating GaAs

B.1.4 Wafer SY4

This heterostructure was used for adiabatic pumping measurements because of its extrordinarily low ohmic contact resistance. Unfortunately, perhaps due to is very shallow 2DEG, this heterostructure proved too noisy for reliable measurements.
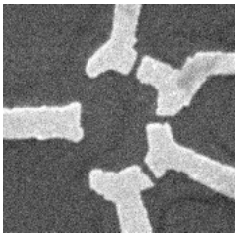
depth	$35\,\mathrm{nm}$
sheet density	$n = 7.3 \times 10^{11}\,\mathrm{cm}^{-2}$
mobility	$\mu = 0.14 \times 10^6\,\mathrm{cm}^2/\mathrm{V\,s}$
ohmic contacts	$R \approx 10\text{–}40\,\Omega$

50 Å	GaAs Cap
138 Å	$Al_{0.3}Ga_{0.7}As$
18 Å	Si modulation doped regoin
143 Å	$Al_{0.3}Ga_{0.7}As$ spacer
	GaAs

B.2 Devices

The following devices produced published data:

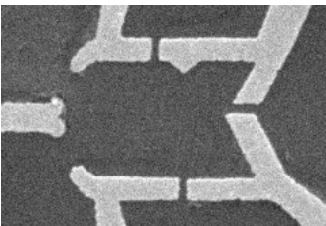### B.2.1 Insomnia 6–13, 7–5

1 μm ⊢———⊣

Area = $0.4\,\mu\mathrm{m}^2$

2DEG: 940708A

Experiment: Dephasing (both dots)

B.2.2 Insomnia 7–7

1 μm ⊢———⊣

Area = $1.9\,\mu\mathrm{m}^2$
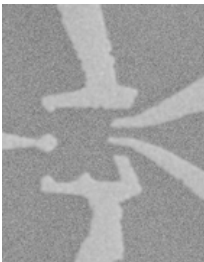
2DEG: 940708A

Experiment: Dephasing

B.2.3   Insomnia 7–4
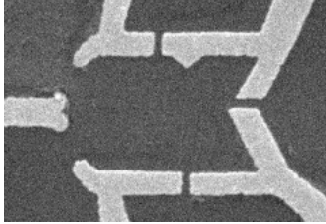
1 μm ⊢⎯⎯⎯⊣

Area = $4.0\,\mu\mathrm{m}^2$

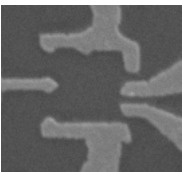2DEG: 940708A

Experiment: Dephasing, High Bias Transport

B.2.4   Gibraltar 2–8

1 μm ⊢⎯⎯⎯⊣

Area = $0.45\,\mu\mathrm{m}^2$

2DEG: 960924C

Experiment: Adiabatic Pumping
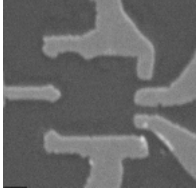
B.2.5   Tanzania 2–13

1 μm ⊢⎯⎯⊣

Area = $0.48\,\mu\mathrm{m}^2$

2DEG: 931217B

Experiment: Adiabatic Pumping

B.2.6   Tanzania 2–19

1 μm ⊢────┤

Area = $0.56\,\mu\mathrm{m}^2$

2DEG: 931217B

Experiment: Adiabatic Pumping

B.2.7   MS990516 2
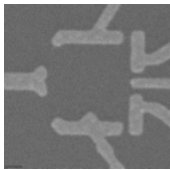
1 μm ⊢────┤

Area = $0.49\,\mu\mathrm{m}^2$

2DEG: SY4

Experiment: Adiabatic Pumping

Appendix C

Radio Frequency Heat Sinks

One of the experimental challenges faced in the pumping experiments was connecting the high frequency (20 MHz) radiation to the gates of the dot. Three considerations were important:

- transmission of the radiation with low loss

- localization of the radiation to the gates

- maintenance of the base temperature and hold time of the cryostat

At first, two semi-rigid coaxial cables (stainless inner conductor, CuBe outer jacket) were installed directly from the top of the cryostat to the chip carrier socket. Heat sinking of the outer conductor was accomplished by wrapping with bare copper wire connected to the cryostat at each temperature stage (4 K, 1 K, and at the ^{3}He pot). The inner conductor was not thermally connected to the cryostat except at the chip carrier socket. While this arrangement delivered the radiation to the gates and produced some encouraging electron pumping results, the lack of heat sinking raised the base temperature from ~ 300 mK to ~ 400 mK with a resulting reduction in hold time from about 12 hours to only 2 hours. This short hold time made serious experiments difficult.

To correct this large heat leak, a heat sink was designed for both inner and outer conductors of the coaxial cable. With advice from Michael Roukes at Caltech, we designed the heat sink shown in figure C.1 which was fabricated in Cu by the physics department machine shop. The heart of the heat sink is a strip line conductor composed of Au on a sapphire substrate chosen for its high thermal conductivity. Two strips are fabricated on
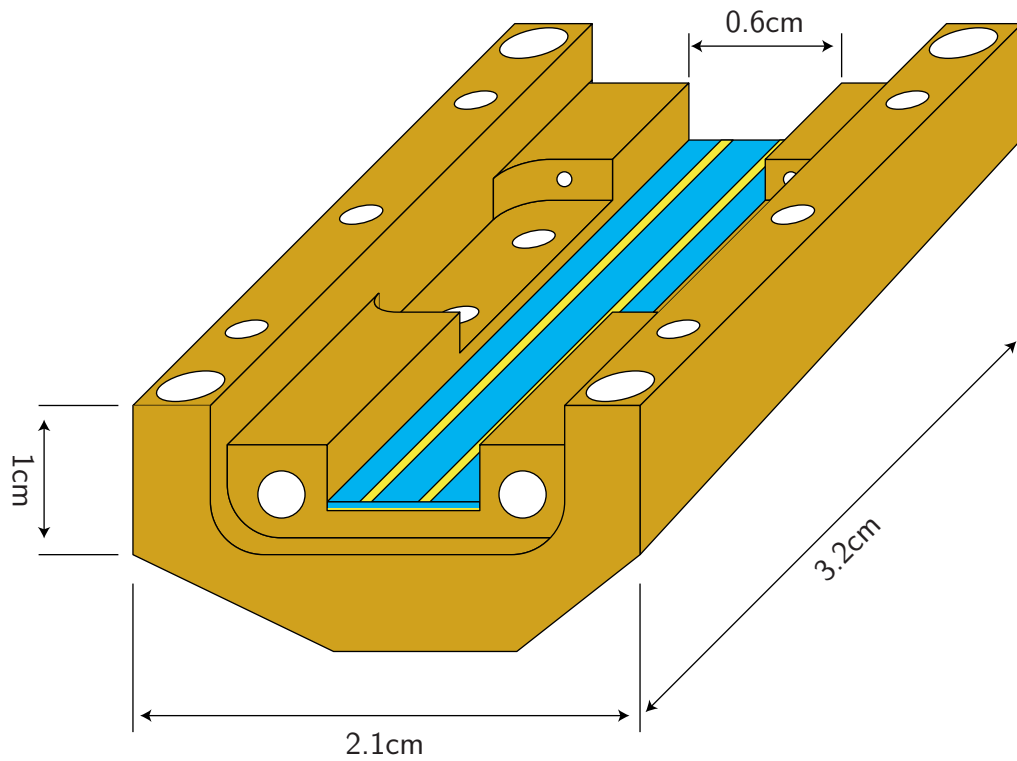
Figure C.1: Schematic drawing of the coaxial heat sink showing the Cu main body with the bottom sapphire substrate (blue) and Au stripline conductors installed. The heat sink is completed by the second sapphire substrate along with two CuBe clips which hold the stripline in place, and two end caps and a top which screw into the holes shown.

one side of a sapphire substrate 0.02 in thick with an optical lift-off process (see sections A.2) and the back of the substrate is coated with gold. This substrate is placed in the trench at the center of the heat sink and semi-rigid coaxial cable (0.34 in. diameter stainless steel center conductor and shield) is connected to the strips with silver epoxy (Epo-Tek 410). Note that this joint came loose due to thermal expansion and caused the destruction of several devices. It was repaired with more silver epoxy and has caused no problems in over a year of use. With the connections in place, another Au coated sapphire substrate is placed, Au side up, on top of the strips, completing the strip line. The whole sandwich is held in place by two CuBe clips which also serve to ground the top Au layer, and a top (not shown in figure C.1) which mates tightly to the heat sink body. Note that two heat sinks were fabricated by the machine shop and the second heat sink was never assembled. The parts including the Cu body and the blank sapphire substrates remain as of this writing in my sample drawer in McCullough 015.

The heat sink is bolted to the 1 K pot of the cryostat and connected to semi-rigid coax from the top of the cryostat and to the sample. The outer conductor of the coax is also connected to the cryostat at the 4 K stage by passing it through a Cu plate connected to the top of the cryostat. At the sample end, the center conductor of each coax is connected to one of the pins on the chip carrier socket with the shield coming as close to the connection as possible.

In this configuration, the cryostat performed very well with base temperatures around 330 mK and an 8 hour hold time. The high frequency signal reached the chip carrier without significant attenuation at 20 MHz and the two signals were quite uniform. No attempt was made to test at higher frequencies.

Bibliography

[1] O. Agam, The magnetic response of chaotic mesoscopic systems, *J. Phys. I (Paris)* **4**, 697 (1994).

[2] O. Agam and S. Fishman, Semiclassical analysis of energy level correlations for a disordered mesoscopic system, *Phys. Rev. Lett.* **76**, 726 (1996).

[3] B. L. Al'tshuler, Fluctuations in the extrinsic conductivity of disordered conductors, *Pis'ma Zh. Eksp. Teor. Fiz.* **41**, 530 (1985). [JTEP Lett. **41**, 648 (1985)].

[4] B. L. Al'tshuler and A. Aronov, Electron-electron interaction in disordered conductors, in *Electron-Electron Interactions in Disordered Systems*, A. Efros and M. Pollak, eds. (Elsevier, Amsterdam, 1985), pp. 1–153.

[5] B. L. Al'tshuler, M. E. Gershenson, and I. L. Aleiner, Phase relaxation of electrons in disordered conductors, *Physica E* **3**, 58 (1998).

[6] B. L. Al'tshuler and L. I. Glazman, Pumping electrons, *Science* **283**, 1864 (1999).

[7] N. Argaman, Semiclassical analysis of the quantum interference corrections to the conductance of mesoscopic systems, *Phys. Rev. B* **53**, 7035 (1996).

[8] N. W. Ashcroft and N. D. Mermin, *Solid State Physics* (Saunders College, Philadelphia, 1976).

[9] J. E. Avron, personal communication (1998).

[10] H. U. Baranger, R. A. Jalabert, and A. D. Stone, Weak localization and integrability in ballistic cavities, *Phys. Rev. Lett.* **70**, 3876 (1993).

[11] H. U. Baranger and P. A. Mello, Mesoscopic transport through chaotic cavities: a random S-matrix theory approach, *Phys. Rev. Lett.* **73**, 142 (1994).

[12] H. U. Baranger and P. A. Mello, Effect of phase breaking on quantum transport through chaotic cavities, *Phys. Rev. B* **51**, 4703 (1995).

[13] R. E. Bartolo, N. Giordano, X. Huang, and G. H. Bernstein, h/e Aharonov-Bohm photovoltaic oscillations in mesoscopic Au rings, *Phys. Rev. B* **55**, 2384 (1997).

[14] C. W. J. Beenakker, Random-matrix theory of quantum transport, *Rev. Mod. Phys.* **69**, 731 (1997).

[15] C. W. J. Beenakker and H. Van Houten, Quantum transport in semiconductor nanostructures, in *Solid State Physics*, H. Ehrenreich and D. Turnbull, eds. (Academic Press, San Diego, 1991), vol. 44, pp. 1–228.

[16] V. Belincher and I. Sturman, The photogalvanic effect in media lacking a center of symmetry, *Sov. Phys. Usp.* **130**, 415 (1980). [Sov. Phys. Usp. **23**, 199 (1980)].

[17] J. P. Bird, K. Ishibashi, D. K. Ferry, Y. Ochiai, Y. Aoyagi, and T. Sugano, Phase breaking in ballistic quantum dots: transition from two- to zero-dimensional behavior, *Phys. Rev. B* **51**, 18037 (1995).

[18] P. W. Brouwer, Scattering approach to parametric pumping, *Phys. Rev. B* **58**, 10135 (1998).

[19] P. W. Brouwer and C. W. J. Beenakker, Effect of a voltage probe on the phase-coherent conductance of a ballistic chaotic cavity, *Phys. Rev. B* **51**, 7739 (1995).

[20] P. W. Brouwer and C. W. J. Beenakker, Voltage-probe and imaginary-potential models for dephasing in a chaotic quantum dot, *Phys. Rev. B* **55**, 4695 (1997).

[21] P. W. Brouwer, K. M. Frahm, and C. W. J. Beenakker, Quantum mechanical time-delay matrix in chaotic scattering, *Phys. Rev. Lett.* **78**, 4737 (1997).

[22] M. Büttiker, Role of quantum coherence in series resistors, *Phys. Rev. B* **33**, 3020 (1986).

[23] M. Büttiker, H. Thomas, and A. Prêtre, Curent partition in multiprobe conductors in the presence of slowly oscillating external potentials, *Z. Phys. B* **94**, 133 (1994).

[24] I. H. Chan, R. M. Clarke, C. M. Marcus, K. Campman, and A. C. Gossard, Ballistic conductance fluctuations in shape space, *Phys. Rev. Lett.* **74**, 3876 (1995).

[25] A. M. Chang, H. U. Baranger, L. N. Pfeiffer, and K. W. West, Weak localization in chaotic versus nonchaotic cavities: a striking difference in the line shape, *Phys. Rev. Lett.* **73**, 2111 (1994).

[26] A. M. Chang, H. U. Baranger, L. N. Pfeiffer, K. W. West, and T. Y. Chang, Non-gaussian distribution of Coulomb blockade peak heights in quantum dots, *Phys. Rev. Lett.* **76**, 1695 (1996).

[27] K. K. Choi, D. C. Tsui, and K. Alavi, Dephasing time and one-dimensional localization of two-dimensional electrons in $GaAs/Al_xGa_{1-x}As$ heterostructures, *Phys. Rev. B* **36**, 7751 (1987).

[28] R. M. Clarke, I. H. Chan, C. M. Marcus, C. I. Duruöz, J. S. Harris Jr., K. Campman, and A. C. Gossard, Temperature dependence of phase breaking in ballistic quantum dots, *Phys. Rev. B* **52**, 2656 (1995).

[29] Conductus Inc., Typical performance parameters of the s165c dc squid (1997).

[30] S. M. Cronenwett, S. M. Maurer, S. R. Patel, C. M. Marcus, C. I. Duruöz, and J. S. Harris Jr., Mesoscopic coulomb blockade in one-channel quantum dots, *Phys. Rev. Lett.* **81**, 5904 (1998).

[31] E. Doron, U. Smilansky, and A. Frenkel, Chaotic scattering and transmission fluctuations, *Physica D* **50**, 367 (1991).

[32] P. M. Echternach, M. E. Gershenson, and H. M. Bozler, Nyquist phase relaxation in one-dimensional metal films, *Phys. Rev. B* **48**, 11516 (1993).

[33] K. B. Efetov, Temperature effects in quantum dots in the regime of chaotic dynamics, *Phys. Rev. Lett.* **74**, 2299 (1995).

[34] V. I. Fal'ko, Nonlinear properties of mesoscopic junctions under high-frequency field irradiation, *Europhys. Lett.* **8**, 785 (1989).

[35] V. I. Fal'ko and D. E. Khmel'nitskiĭ, Mesoscopic photovoltaic effect in microjunctions, *Zh. Eksp. Teor. Fiz.* **95**, 328 (1989). [Sov. Phys. JTEP **68**, 186 (1989)].

[36] D. S. Fisher and P. A. Lee, Relation between conductivity and transmission matrix, *Phys. Rev. B* **23**, 6851 (1981).

[37] K. Flensberg and A. A. Odintsov, Towards single-electron metrology, *cond-mat/9908219* (1999).

[38] J. A. Folk and C. M. Marcus, personal communication (1999).

[39] J. A. Folk, S. R. Patel, S. F. Godijn, A. G. Huibers, S. M. Cronenwett, C. M. Marcus, K. Campman, and A. C. Gossard, Statistics and parametric correlations of Coulomb blockade peak fluctuations in quantum dots, *Phys. Rev. Lett.* **76**, 1699 (1996).

[40] H. Fukuyama and E. Abrahams, Inelastic scattering time in two-dimensional disordered metals, *Phys. Rev. B* **27**, 5976 (1983).

[41] A. K. Geim, I. V. Grigorieva, J. G. S. Lok, J. C. Maan, S. V. Dubonos, X. Q. Li, F. M. Peeters, and Y. V. Nazarov, Precision magnetometry on a submicron scale: Magnetisation of superconducting quantum dots, *Superlattices and Microstructures* **23**, 151 (1996).

[42] G. F. Giuliani and J. J. Quinn, Lifetime of a quasiparticle in a two-dimensional electron gas, *Phys. Rev. B* **26**, 4421 (1982).

[43] D. Gottesman, *Stabilizer Codes and Quantum Error Correction*, Ph.D. thesis, California Institute of Technology (1997).

[44] A. Greiner, L. Reggiani, T. Kuhn, and L. Varani, Thermal conductivity and Lorenz number for one-dimensional ballistic transport, *Phys. Rev. Lett.* **78**, 1114 (1997).

[45] L. K. Grover, Quantum mechanics helps in searching for a needle in a haystack, *Phys. Rev. Lett.* **79**, 325 (1997).

[46] V. L. Gurevich, Heat generation by electric current in nanostructures, *Phys. Rev. B* **55**, 4522 (1997).

[47] M. A. Herman and H. Sitter, *Molecular Beam Epitaxy: Fundamentals and Current Status* (Springer-Verlag, New York, 1996), 2nd ed.

[48] A. G. Huibers, *Electron Transport and Dephasing in Semiconductor Quantum Dots*, Ph.D. thesis, Stanford University (1999).

[49] A. G. Huibers, S. R. Patel, C. M. Marcus, P. W. Brouwer, C. I. Duruöz, and J. S. Harris Jr., Distributions of the conductance and its parametric derivatives in quantum dots, *Phys. Rev. Lett.* **81**, 1917 (1998).

[50] A. G. Huibers, M. Switkes, C. M. Marcus, K. Campman, and A. C. Gossard, Dephasing in open qauntum dots, *Phys. Rev. Lett.* **81**, 200 (1997).

[51] Y. Imry and A. Stern, Dephasing by coupling with the environment, application to Coulomb electron-electron interactions in metals, *Semicond. Sci. Technol.* **9**, 1879 (1994).

[52] J. D. Jackson, *Classical Electrodynamics* (Wiley, New York, 1999), 3rd ed.

[53] R. A. Jalabert, H. U. Baranger, and A. D. Stone, Conductance fluctuations in the ballistic regime: a probe of quantum chaos?, *Phys. Rev. Lett.* **65**, 2442 (1990).

[54] R. A. Jalabert, J.-L. Pichard, and C. W. J. Beenakker, Universal quantum signatures of chaos in ballistic transport, *Europhys. Lett.* **27**, 255 (1994).

[55] R. A. Jalabert, A. D. Stone, and Y. Alhassid, Statistical theory of Coulomb blockade oscillations: quantum chaos in quantum dots, *Phys. Rev. Lett.* **68**, 3468 (1992).

[56] A. T. Johnson, L. P. Kouwenhoven, W. de Jong, N. C. van der Vaart, C. J. P. M. Harmans, and C. T. Foxon, Zero-dimensional states and single electron charging in quantum dots, *Phys. Rev. Lett.* **69**, 1592 (1992).

[57] T. Jungwirth and A. H. MacDonald, Electron-electron interactions and two-dimensional–two-dimensional tunneling, *Phys. Rev. B* **53**, 7403 (1996).

[58] M. W. Keller, A. L. Eichenberger, J. M. Martinis, and N. M. Zimmerman, A capacitance standard based on counting electrons, *Science* **285**, 1706 (1999).

[59] M. W. Keller, J. M. Martinis, and R. L. Kautz, Rare errors in a well-characterized electron pump: Comparison of experiment and theory, *Phys. Rev. Lett.* **80**, 4530 (1998).

[60] Y. B. Khavin, M. E. Gershenson, and A. L. Bogdanov, Decoherence and the Thouless crossover in one-dimensional conductors, *Phys. Rev. Lett.* **81**, 1066 (1998).

[61] L. P. Kouwenhoven, S. Jauhar, K. McCormick, D. Dixon, P. L. McEuen, Y. V. Nazarov, N. C. van der Vaart, and C. T. Foxon, Photon-assisted tunneling through a quantum dot, *Phys. Rev. B* **50**, 2019 (1994).

[62] L. P. Kouwenhoven, S. Jauhar, J. Orenstein, P. L. McEuen, Y. Nagamune, J. Motohisa, and H. Sakaki, Observation of photon-assisted tunneling through a quantum dot, *Phys. Rev. Lett.* **73**, 3443 (1994).

[63] L. P. Kouwenhoven, A. T. Johnson, N. C. van der Vaart, C. J. P. M. Harmans, and C. T. Foxon, Quantized current in a quantum-dot turnstile using oscillating tunnel barriers, *Phys. Rev. Lett.* **67**, 1626 (1991).

[64] L. P. Kouwenhoven, A. T. Johnson, N. C. van der Vaart, A. van der Enden, C. J. P. M. Harmans, and C. T. Foxon, Quantized current in a quantum dot turnstile, *Z. Phys. B* **85**, 381 (1991).

[65] L. P. Kouwenhoven, C. M. Marcus, P. L. McEuen, S. Tarucha, R. M. Westervelt, and N. S. Wingreen, Electron transport in quantum dots, in *Proceedings of the Advanced Study Institute on Mesoscopic Electron Transport*, L. P. Kouwenhoven, G. Schön, and L. L. Sohn, eds. (Kluwer, Dordrecht, 1997), Nato ASI Series E: Applied Sciences.

[66] A. Kumar, L. Saminadayar, D. C. Glattli, Y. Jin, and B. Etienne, Experimental test of the quantum shot noise reduction theory, *Phys. Rev. Lett.* **76**, 2778 (1996).

[67] C. Kurdak, A. M. Chang, A. Chin, and T. Y. Chang, Quantum interference effects and spin-orbit interaction in quasi-one-dimensional wires and rings, *Phys. Rev. B* **46**, 6846 (1992).

[68] R. Landauer, Spatial variation of currents and fields due to localized scatterers in metallic conduction, *IBM J. Res.* **1**, 223 (1957).

[69] P. A. Lee and A. D. Stone, Universal conductance fluctuations in metals, *Phys. Rev. Lett.* **55**, 1622 (1985).

[70] P. A. Lee, A. D. Stone, and H. Fukuyama, Universal conductance fluctuations in metals: Effects of finite temperature, interactions, and magnetic field, *Phys. Rev. B* **35**, 1039 (1987).

[71] J. Lin and N. Giordano, Observation of the Nyquist phase-coherence time in thin Au-Pd wires, *Phys. Rev. B* **33**, 1519 (1986).

[72] H. Linke, J. P. Bird, J. Cooper, P. Omling, Y. Aoyagi, and T. Sugano, Phase breaking of non-equilibrium electrons in a ballistic qauntum dot, *Phys. Rev. B* **56**, 14937 (1997).

[73] J. Liu, M. A. Pennington, and N. Giordano, Mesoscopic photovoltaic effect, *Phys. Rev. B* **45**, 1267 (1992).

[74] C. Marcus, I. Chan, R. Clarke, K. Kampman, and A. Gossard, Statistics of conductance fluctuations in quantum dots, in *Quantum Dynamics of Submicron Structures*, H. Cerdeira and B. Kramer, eds. (Kluwer, Dordrecht, 1995).

[75] C. M. Marcus, S. R. Patel, A. G. Huibers, S. M. Cronenwett, M. Switkes, I. H. Chan, R. M. Clarke, J. A. Folk, S. F. Godijn, K. Campman, and A. C. Gossard, Quantum chaos in open versus closed quantum dots: Signatures of interacting particles, *Chaos, Solitons, & Fractals* **8**, 1261 (1997).

[76] C. M. Marcus, A. J. Rimberg, R. M. Westervelt, P. F. Hopkins, and A. C. Gossard, Conductance fluctuations and chaotic scattering in ballistic microstructures, *Phys. Rev. Lett.* **69**, 506 (1992).

[77] C. M. Marcus, R. M. Westervelt, P. F. Hopkins, and A. C. Gossard, Phase breaking in ballistic quantum dots: experiment and analysis based on chaotic scattering, *Phys. Rev. B* **48**, 2460 (1993).

[78] A. Mittal, Electron-phonon scattering rates in 2D systems, in *Quantum Transport in Submicron Structures*, B. Kramer, ed. (Kluwer, Dordrecht, 1996), vol. 326 of *Nato ASI Series E: Applied Sciences*, pp. 303–313.

[79] A. Mittal, R. G. Wheeler, M. W. Keller, D. E. Prober, and R. N. Sacks, Electron-phonon scattering rates in GaAs/AlGaAs 2DEGs below 0.5 k, *Surf. Sci.* **361–362**, 537 (1996).

[80] P. Mohanty, E. M. Q. Jariwala, and R. A. Webb, Intrinsic decoherence in mesoscopic systems, *Phys. Rev. Lett.* **78**, 3366 (1997).

[81] P. Mohanty and R. A. Webb, Decoherence and quantum fluctuations, *Phys. Rev. B* **55**, R13452 (1997).

[82] L. W. Molenkamp, T. Gravier, H. van Houten, O. J. A. Buijk, M. A. A. Mabesoone, and C. T. Foxon, Peltier coefficient and thermal conductance of a quantum point contact, *Phys. Rev. Lett.* **68**, 3765 (1992).

[83] S. Q. Murphy, J. P. Eisenstein, L. N. Pfeiffer, and K. W. West, Lifetime of two-dimensional electrons measured by tunneling spectroscopy, *Phys. Rev. B* **52**, 14825 (1995).

[84] T. H. Oosterkamp, L. P. Kouwenhoven, A. E. A. Koolen, N. C. van der Vaart, and C. J. P. M. Harmans, Photon-assisted tunneling through a quantum dot, *Semicond. Sci. Technol.* **11**, 1512 (1996).

[85] T. H. Oosterkamp, L. P. Kouwenhoven, A. E. A. Koolen, N. C. van der Vaart, and C. J. P. M. Harmans, Photon sidebands of the ground state and first excited state of a quantum dot, *Phys. Rev. Lett.* **76**, 1536 (1997).

[86] D. Pines and P. Nozieres, *Theory of quantum liquids*, vol. 1 (W. A. Benjamin, New York, 1989).

[87] Z. Pluhař, H. A. Weidenmuller, J. A. Zuk, and C. H. Lewenkopf, Suppression of weak localization due to magnetic flux in few-channel ballistic microstructures, *Phys. Rev. Lett.* **73**, 2115 (1994).

[88] H. Pothier, P. Lafarge, P. F. Orfilia, C. Urbina, C. Esteve, and M. H. Devoret, Single electron pump fabricated with ultrasmall normal tunnel junctions, *Physica B* **169**, 573 (1991).

[89] H. Pothier, P. Lafarge, C. Urbina, D. Esteve, and M. H. Devoret, Single-electron pump based on charging effects, *Europhys. Lett.* **17**, 249 (1992).

[90] C. R. Proetto, Heat conduction through ballistic quantum-point contacts: quantized steps in the thermal conductance, *Solid State Comm.* **80**, 909 (1991).

[91] B. Reulet, H. Bouchiat, and D. Mailly, Magnetoconductance, weak localization and electron-electron interactions in semi-ballistic quantum wires, *Europhys. Lett.* **31**, 305 (1995).

[92] M. Rokni and Y. Levinson, Joule heat in point contacts, *Phys. Rev. B* **52**, 1882 (1995).

[93] J. J. Sakurai, *Modern Quantum Mechanics* (Addison-Wesley, Reading, Mass., 1995).

[94] P. Schor, Polynomial-time algorithms for prime factorization and discrete logarithms on a quantum computer, *SIAM J. Computing* **26**, 1484 (1997).

[95] U. Sivan, Y. Imry, and A. G. Aronov, Quasi-particle lifetime in a quantum dot, *Europhys. Lett.* **28**, 115 (1994).

[96] U. Sivan, F. P. Milliken, K. Milkove, S. Rishton, Y. Lee, J. M. Hong, V. Boegli, D. Kern, and M. DeFranza, Spectroscopy, electron-electron interaction, and level statistics in a disordered quantum dot, *Europhys. Lett.* **25**, 605 (1994).

[97] U. Smilansky, The classical and quantum theory of chaotic scattering, in *Chaos and Quantum Physics*, M.-J. Giannoni, A. Voros, and J. Zinn-Justin, eds. (Elsevier, Amsterdam, 1990), p. 371.

[98] B. Spivak, F. Zhou, and M. T. Beal Monod, Mesoscopic mechanisms of the photovoltaic effect and microwave absorption in granular metals, *Phys. Rev. B* **51**, 13226 (1995).

[99] A. Steane, Quantum computing, *Rep. Prog. Phys.* **61**, 117 (1998).

[100] D. R. Stewart, D. Sprinzak, C. M. Marcus, C. I. Duruöz, and J. S. Harris Jr., Correlations between ground and excited state spectra of a quantum dot, *Science* **278**, 1784 (1997).

[101] M. Switkes, A. G. Huibers, C. M. Marcus, K. Campman, and A. C. Gossard, High bias transport and magnetometer design in open quantum dots, *Appl. Phys. Lett.* **72**, 471 (1998).

[102] M. Switkes, C. M. Marcus, K. Campman, and A. C. Gossard, An adiabatic quantum electron pump, *Science* **283**, 1905 (1999).

[103] V. I. Talyanskii, J. M. Shilton, M. Pepper, C. G. Smith, C. J. B. Ford, E. H. Linfield, D. A. Ritchie, and G. A. C. Jones, Single-electron transport in a one-dimensional channel by high-frequency surface acoustic waves, *Phys. Rev. B* **56**, 15180 (1997).

[104] S. Tarucha, D. G. Austing, T. Honda, R. J. van der Hage, and L. P. Kouwenhoven, Shell filling and spin effects in a few electron quantum dot, *Phys. Rev. Lett.* **77**, 3613 (1996).

[105] D. J. Thouless, Quantization of particle transport, *Phys. Rev. B* **27**, 6083 (1983).

[106] B. J. van Wees, H. van Houten, C. W. J. Beenakker, J. G. Williamson, L. P. Kouwenhoven, D. van der Marel, and C. T. Foxon, Quantized conductance of point contacts in a two-dimensional electron gas, *Phys. Rev. Lett.* **60**, 848 (1988).

[107] D. A. Wharam, T. J. Thornton, R. Newbury, M. Pepper, H. Ahmed, J. E. F. Frost, D. G. Hasko, D. C. Peacock, D. A. Ritchie, and G. A. C. Jones, One-dimensional transport and the quantisation of the ballistic resistance, *J. Phys. C* **21**, L209 (1988).

[108] A. Yacoby, M. Heiblum, D. Mahalu, and H. Shtrikman, Coherence and phase sensitive measurements in a quantum dot, *Phys. Rev. Lett.* **74**, 4047 (1995).

[109] A. Yacoby, M. Heiblum, H. Shtrikman, V. Umansky, and D. Mahalu, Dephasing of ballistic electrons as a function of temperature and carrier density, *Semicond. Sci. Technol.* **9**, 907 (1994).

[110] A. Yacoby, U. Sivan, C. P. Umbach, and J. M. Hong, Interference and dephasing by electron-electron interaction on length scales shorter than the elastic mean free path, *Phys. Rev. Lett.* **66**, 1938 (1991).

[111] L. Zheng and S. Das Sarma, Coulomb scattering lifetime of a two-dimensional electron gas, *Phys. Rev. B* **53**, 9964 (1996).

[112] F. Zhou, personal communication (1998).

[113] F. Zhou, B. Spivak, and B. L. Altshuler, Mesoscopic mechanism of adiabatic charge transport, *Phys. Rev. Lett.* **82**, 608 (1999).